INCUBATION OF CONTINUOOLITHUS CANADENSIS EGGS FROM THE LATE CRETACEOUS TWO MEDICINE FORMATION OF MONTANA

by

Rebecca Joy Schaff

A thesis submitted in partial fulfillment
of the requirements for the degree

of

Master of Science

in

Earth Sciences

MONTANA STATE UNIVERSITY
Bozeman, Montana

May 2012

©COPYRIGHT

by

Rebecca Joy Schaff

2012

All Rights Reserved

APPROVAL

of a thesis submitted by

Rebecca Joy Schaff

This thesis has been read by each member of the thesis committee and has been found to be satisfactory regarding content, English usage, format, citation, bibliographic style, and consistency and is ready for submission to The Graduate School.

Dr. Frankie Jackson

Approved for the Department of Earth Sciences

Dr. David Mogk

Approved for The Graduate School

Dr. Carl A. Fox

STATEMENT OF PERMISSION TO USE

In presenting this thesis in partial fulfillment of the requirements for a master's degree at Montana State University, I agree that the Library shall make it available to borrowers under rules of the Library.

If I have indicated my intention to copyright this thesis by including a copyright notice page, copying is allowable only for scholarly purposes, consistent with "fair use" as prescribed in the U.S. Copyright Law. Requests for permission for extended quotation from or reproduction of this thesis in whole or in parts may be granted only by the copyright holder.

Rebecca Joy Schaff

May, 2012

ACKNOWLEDGEMENTS

I thank my advisor F. Jackson for her amazing patience in helping to edit this thesis and for the guidance she has offered me while a student at MSU. I thank J. Horner and the Paleontology Department at the Museum of the Rockies for access to collections, for supporting fieldwork related to this thesis, and for use of the Gabriel Laboratory for Cellular and Molecular Paleontology. I thank additional members of my thesis committee, D. Varricchio and J. Schmitt for their time and efforts in editing my thesis and offering advice. I thank B. Jackson for reviewing early drafts of this thesis and offering valuable insights into methods of water vapor calculation and statistical analysis. I thank the staff of the Imaging and Chemical Analysis Laboratory (ICAL) at Montana State University for use of equipment and technical advice, and D. Mogk for training on ICAL equipment. I thank D. Lageson for assistance with laboratory techniques for analysis of carbonate rocks. I thank M. and T. Kohler for their continued support of fieldwork at Egg Mountain and the Willow Creek anticline. I thank D. Varricchio for support provided through his National Science Foundation grant (0847777 (EAR)) for field work at Egg Mountain. I thank Carrie Gottschalk for help editing and Jason Moore for guidance regarding field techniques. Lastly, I thank the field crews who excavated Egg Mountain over the years and collected the samples used in this study.

TABLE OF CONTENTS

1. INTRODUCTION 1

Egg and Clutch Geometry 2
Trace Fossil Nests 3
Water Vapor Conductance 6
Purpose of the Study 6

2. GEOLOGY 8

Tectonic Setting 8
Review of Fossil Egg Locality and Materials 8

3. MATERIALS AND METHODS 12

Nesting Trace 12
Preparation of Nesting Trace 12
Thin Sections 15
Total Organic Carbon 16
X-Ray Diffraction (XRD) 16
Energy Dispersive Spectra (EDS) 17
Rock Slabs 18
Eggs and Clutch 18
Eggshell Preparation 21
Scanning Electron Microscope 23
Water Vapor Conductance (GH2O) 23

4. DESCRIPTION 25

Sedimentology and Stratigraphy 25
Nesting Trace 25
Total Organic Carbon 29
Iron Staining 30
X-Ray Diffraction 33
Energy Dispersive Spectroscopy 34
Eggs and Eggshell 39
Gross Egg Morphology 39
Microstructure 39
Entire Sample Thickness 40
Eggshells with Intact Mammillary Layers 41

TABLE OF CONTENTS – CONTINUED

Thickness of Idealized Sample Set 41
Pore Area and Density 46
Water Vapor Conductance 47
Entire Sample GH2O 55
GH2O Excluding Incomplete Samples 55
GH2O of Idealized Sample Set 56

5. DISCUSSION 60

6. CONCLUSIONS 75

REFERENCES CITED 77

APPENDIX A: Tables 83

LIST OF TABLES

Table Page

1. Description of Specimens 84

2. Completeness of Eggs....85

3. Tangential Section Measurements 86

4. Variables and Constants....87

5. Calculations for GH2O 88

6. Regional Measurements of Microstructures 89

7. Sediment Characteristics / Comparison 90

8. Completeness of Sample Mammillary Layer 91

LIST OF FIGURES

Figure Page

1. Trace Fossil Nests 5

2. Location of the Two Medicine Formation 11

3. Excavation of MOR 3062 13

4. Microstratigraphic Section of MOR 3062 Trace 14

5. Photo of Cross-Section of Trace 15

6. *Continuoolithus canadensis* Eggs 20

7. Egg Gross Morphology 21

8. MOR 3062-S-N Nodules 27

9. Superimposed Eggshell Fragments 28

10. MOR 3062-S-O and MOR 3062-S-F2 28

11. Organic Material from Trace 29

12. Iron Stained Sediment (MOR 3062-S-U3, N) 31

13. Iron Stained Sediment (MOR 3062-S-F1, O, F2) 32

14. XRD Sediment Results 34

15. EDS for Red mudstone (MOR-S-U3) 35

16. EDS for Red mudstone (MOR-S-N) 36

17. EDS for Red mudstone (MOR-S-F1) 37

18. EDS for Green mudstone (MOR-S-O) 38

19. SEM Images of Mammillary and Continuous Shell Layers 42

LIST OF FIGURES – CONTINUED

Figure Page

20. Histograms of Shell Thickness 43

21. Shell Thickness Histogram for MOR 326A & B 44

22. Shell Thickness Histogram for MOR 326C & MOR 301B 44

23. Shell Thickness Histogram for YPM-PU 22544 & MOR 3062A 45

24. SEM Images of Mineral-filled Pores and Altered Shell 45

25. Thin Section Showing Pore 47

26. Mammillary Layer of MOR 326A 48

27. Mammillary Layer of MOR 326B 49

28. Mammillary Layer of MOR 326C 50

29. Mammillary Layer of MOR 301B 51

30. Mammillary Layer of MOR 3062A 52

31. Mammillary Layer of YPM-PU 22544 53

32. Histogram of Pore Area and Density 54

33. Histogram of GH2O for MOR 326A & MOR 326B 57

34. Histogram of GH2O for MOR 326C & MOR 301B 57

35. Histogram of GH2O for MOR 3062A & YPM-PU 22544 58

36. Histograms of Total Egg and Regional GH2O 59

37. Nesting Trace Process Illustration 65

38. Photo of MOR 326 Clutch 68

GLOSSARY OF INSTITUTIONAL ABBREVIATIONS

MOR:	Museum of the Rockies
YPM-PU:	Princeton University

ABSTRACT

Incubation strategies of extinct organisms are largely speculative. Most inferences of nesting behavior are based on comparison with closely related extant taxa. To date the most useful evidence for support of a particular incubation strategy includes water vapor conductance (determined from fossil eggshell) and sedimentary structures, associated with eggs or eggshell, that are interpreted as fossil nests. One such sedimentary structure (MOR 3062) from the Upper Cretaceous Two Medicine Formation of Montana, is described along with the microstructure of the associated eggs and eggshell (oospecies *Continuoolithus canadensis*). The green nest trace truncates red mudstone and differs in sedimentary attributes. Geochemical analysis indicates that the host substrate was highly oxidized compared to the in-filled nesting structure. This is probably due to presence of decaying vegetative debris within the structure. A *Continuoolithus canadensis* egg removed from MOR 3062, along with *Continuoolithus canadensis* eggs from the nearby site TM-006, have a water vapor conductance value of 119 mgH^2O/ (day Torr). This equates to a 4.1 times greater mean water vapor conductance in *Continuoolithus canadensis* than a bird egg of the same mass. American alligator (*Alligator mississippensis*) eggs have a water vapor conductance rate 4.2 times greater than a bird egg of the same mass. Strong similarities exist between relative water vapor conductance of *Continuoolithus canadensis* and modern alligators. In addition, characteristics of MOR 3062 suggest the eggs were buried in a mixture of sediment and vegetative debris: therefore, I conclude that *Continuoolithus Canadensis* eggs were incubated under-ground, possibly with the aid of heat produced by rotting vegetation.

INTRODUCTION

Among living amniotes, some turtles and geckos and all archosaurs (i.e., crocodilians and birds) produce hard calcified eggs (Grigg and Beard, 1985; Deeming, 2006). The egg consists of a calcium carbonate shell, organic shell membranes, albumen, yolk, and embryo (Seymour, 1979; Board and Scott, 1980; Grigg and Beard, 1985; Booth and Seymour, 1987). Pores transverse the eggshell and allow passive exchange of water vapor, oxygen, and carbon dioxide between the embryo and the surrounding atmosphere (Board and Scott, 1980).

Studies of eggshell microstructure and water vapor conductance rates in extant bird and reptile eggs support a close relationship between eggshell porosity and microclimate of the nesting environment (Seymour, 1979; Birchard and Kilgore, 1980; Seymour and Ackermann, 1980; Seymour et al., 1986; Booth and Seymour, 1987, Seymour et al., 1987; Booth, 1989). The incubation strategy employed by the adult animal aids in regulating water vapor conductance between the egg and the nest (Seymour and Ackermann, 1980; Deeming, 2002, 2004). For example, most birds' eggs are exposed to the atmosphere and exhibit low conductance rates that minimize water lost to evaporation. In contrast, bird and reptile eggs that are incubated in vegetation mounds, holes, or buried in a substrate exhibit 2-60 times higher water vapor conductance than avian eggs of comparable mass that are sub-aerially exposed and attended by the adult (Seymour and Ackermann, 1980; Booth and Seymour, 1989; Deeming, 2002, 2004). The high conductance values of reptile eggs represent adaption to

high humidity, high CO_2, and low O_2 environments (Seymour and Ackerman, 1980; Deeming and Thompson, 1991).

As in all living archosaurs, non-avian dinosaurs produced rigid eggs comprised of calcium carbonate in the form of calcite (Mikhailov et al., 1996; Zelenitsky et al., 2002). The well-established relationship between water vapor conductance (GH2O) and incubation strategy in extant species has prompted analysis of fossil eggshell microstructure with the goal of understanding incubation strategies of extinct organisms (Seymour, 1979; Williams et al., 1984; Deeming, 2006). Presumably eggs of extinct taxa were subject to similar physiological and environmental constraints as modern eggs. Researchers, therefore, have attempted to infer dinosaur nesting behavior and incubation strategies in order to better understand physiology and reproductive biology. Nesting strategies have been primarily inferred from 1) egg and clutch geometry (Cousin, 1994; Sander et al., 2008; Vila et al., 2009), 2) trace fossil nests (Varricchio et al., 1999; Chiappe et al., 2004) and 3) Calculated water vapor conductance rates (Deeming, 2006 and references therein; Jackson et al., 2008). Here, I review this past research.

Egg and Clutch Geometry

Cousin (1994) reviewed clutch geometries and noted that the spatial distribution of eggs within certain clutches would indicate that they were separated by sediment. Characteristics of such clutches included irregular spacing and vertical distribution within the substrate, random orientation, and small clutch size. Thus, Cousin (1994) proposes

that some dinosaur eggs were incubated in a substrate. Alternately, large circular arrangements of eggs were attributed to sub-aerial incubation (Cousin, 1994).

Sander et al. (2008) reviews sauropod egg clutches from the Late Cretaceous of India, Europe, and South America. This study described two types of clutch geometries. In the first type, eggs are not always in direct contact with one another. They vary in vertical placement within the clutch, are loosely packed, and the lowest egg may not always occur in the centermost point of the clutch. The second type consists of eggs that conform to a bowl-shaped geometry and the lowermost egg is typically in the center of the clutch (Sander et al., 2008). Similarly, Vila et al. (2009) describe clutches from a Late Cretaceous titanosuar egg site on the Iberian Peninsula. The fine grain substrate provided no evidence of a nesting trace. However, taphonomic survey and mapping of clutches revealed clutch geometry similar to that suggested by Sander et al. (2008), which was thought to be indicative of incubation in substrate (Vila et al., 2009).

Trace Fossil Nests

In contrast to clutch geometry, Horner and Makela (1979) used sedimentology to identify the first nesting trace. Horner and Makela (1979) describe a structure (Fig. 1A) from the Cretaceous Two Medicine Formation of Montana containing juvenile *Maiasaura peeblesorum* skeletons and broken eggshell (oospecies *Spheroolithus albertensis*). Brown mudstone was truncated by a green mudstone that formed an oval, bowl-shaped depression containing the skeletal material. Horner and Makela (1979) interpreted this bowl-shaped depression, 2 m wide and 0.75 m deep, as a nest.

Troodon eggs (oospecies *Prismatoolithus levis*) containing embryonic remains also occur in the Upper Cretaceous Two Medicine Formation of Montana (Horner, 1987; Hirsch & Quinn, 1990; Varricchio et al., 1997, 1999). A clutch (MOR 3062) containing 24 eggs occurs within a nesting trace (Fig. 1B; Varricchio et al., 1997, 1999). The trace consisted of a bowl-shaped depression, with an internal area of ~1 m^2. A hard, micritic limestone formed the bowl-shaped depression and a rim that surrounded the clutch; a softer calcareous mudstone filled the depression and covered the nest and eggs. The two litholiogies differed chemically, and the limestone showed evidence of paleosol development. The *Troodon* eggs occurred in the structure, pointed ends down and nearly vertical, partially encased in the lower limestone and covered by the overlying mudstone (Varricchio et al., 1999).

The Auca Mahuevo nesting locality, discovered in the Upper Cretaceous Rio Colorado Formation of Patagonia, Argentina, represents a third example of nesting traces in the fossil record (Chiappe et al., 2000). Eggs (oospecies *Megaloolithus patagonicus*) at Auca Mahuevo are assigned to titanosaur sauropod dinosaurs on the basis of embryonic remains (Chiappe et al., 2003). Chiappe et al. (2004) described six nesting traces. These traces consisted of bowl-shaped depressions that truncated sedimentary structures of sandstone, interpreted as crevasse splay or channel deposits (Fig. 1C). Mudstone, consistent with suspension settling of fine-grained sediments on the floodplain, surrounded the eggs and filled the depressions. Massive sandstone, interpreted as excavated material, formed a raised rim around the depression.

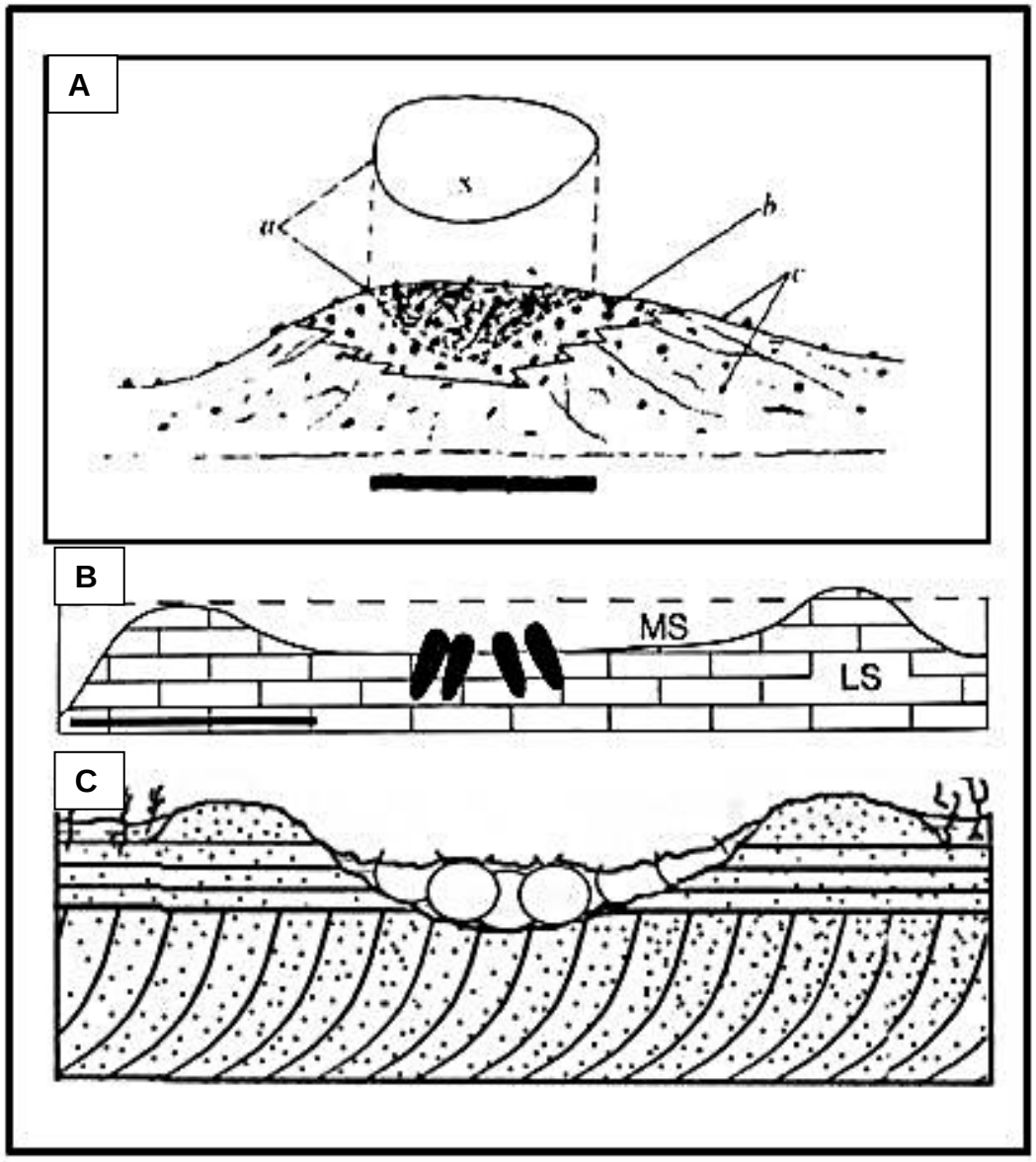


Figure 1. Nesting Traces. A) *Maiasaura* nest (Horner and Makela, 1979). Scale is 2 m. B) *Troodon* nest (Varricchio et al., 1999). Scale is 0.5 m. C) Titanosaurid nest (Chiappe et al., 2004). Scale not given in original figure.

Water Vapor Conductance

Seymour's (1979) seminal study of water vapor conductance of dinosaur eggshell reported conductance values calculated from several eggshell fragments. These conductance rates were compared to those of extant bird and reptile eggs and found to be higher than bird eggs of comparable mass, falling within the range expected for reptile eggs. Later studies (Williams et al., 1984; Sabath, 1991; Deeming, 2002) contributed water vapor conductance values for additional dinosaur eggshell types. Deeming (2006) compiled microstructural measurements of 35 dinosaurian eggshell types from the literature, unpublished communications, and original research. He surveyed water vapor conductance for a wide selection of dinosaurian ootaxa and reported a general trend amongst non-avian dinosaurs for higher water vapor conductance than would be expected for an avian egg of comparable mass.

Purpose of the Study

Although water vapor conductance provides an indicator of incubation environment (Seymour, 1979; Birchard and Kilgore, 1980; Booth, 1989; Deeming, 2006), evidence in the form of nesting trace fossils adds legitimacy to inferences of nesting behavior (Jackson et al., 2008). Ideally, inferences of incubation strategy for extinct taxa should be based on water vapor conductance calculated from fossil eggshell, in combination with sedimentologic and taphonomic study of the nesting locality (Jackson et al., 2008). However, many dinosaur nesting localities occur in fine-grained,

pedogenically modified deposits (e.g. Horner and Makela, 1979; Varricchio et al., 1999; Sander et al., 2008; Vila et al., 2009). The homogeneous nature of the sediment contributes to the difficulty of nest recognition. Although rarely described, trace fossil nests may be more common than appreciated, and failure to recognize these structures may account for their paucity in the fossil record (Chiappe et al., 2004). Few fossil eggs, contained within nesting traces, have been analyzed for GH2O. The study presented here represents the first detailed analysis of a nesting trace (MOR 3062) containing theropod eggs of the ootaxa *Continuoolithus canadensis* from the Two Medicine Formation of Western Montana. I specifically address the following questions in this study:

- Does geochemistry and taphonomy of the MOR 3062 nesting trace provide evidence of nesting site paleoecology and microenvironment of the nest?
- What was the incubation method used by the theropod which constructed the MOR 3062 nesting trace?
- Do the descriptions of *C. canadensis* clutch arrangement, egg gross morphology, and eggshell microstructure in the present study concur with earlier research?
- What is the water vapor conductance rate for *C. canadensis* eggshell? Would this water vapor conductance rate be higher or lower for a bird egg of equal mass?
- Does modification (diagenetic and/or biologic) of *C. canadensis* eggshell significantly affect the calculation of water vapor conductance?
- Does the water vapor conductance value for *C. canadensis* compliment the interpretation of incubation strategy based on the MOR 3062 nesting trace?
- What assumptions and errors may affect findings of this study?

GEOLOGY

Tectonic Setting

The Two Medicine Formation represents proximal terrestrial deposits of the Two Medicine-Judith River clastic wedge resulting from regression of the Late Cretaceous (Campanian) Western Interior Cretaceous Seaway (Gill and Cobban, 1973; Rogers et al., 1993; Rogers, 1998). This 600 meter-thick, non-marine sequence includes materials derived from the Rocky Mountain fold and thrust belt and volcaniclastic deposits associated with the Elkhorn Mountains volcanic center and the Adel volcanic center (Mudge, 1970; Gill and Cobban, 1973; Lorenz, 1981; Lorenz and Gavin, 1984; Rogers et al., 1993; Lageson et al., 2001; Roberts and Hendrix, 2000). Ages of the Two Medicine Formation have been determined from radiometric dating: 80.0 Ma (Rogers et al., 1993) at the Sevenmile Hill locality south of Choteau, 75.5 Ma at the Willow Creek Anticline (Jackson and Varricchio, 2010), and 74.0 Ma near the top of the formation, west of Shelby, Montana (Rogers et al., 1993).

Review of Fossil Locality and Materials

Lorenz and Gavin (1984) described four lithofacies (A-D) comprising the Two Medicine Formation exposed in the Choteau area. Lithofacies D, at the Willow Creek anticline includes a ~ 1 mile^2 area of Two Medicine Formation exposures, and consists of four subfacies:

- A lower subfacies of red and orange siltstone, shale, and gray sandstone, with irregular calcareous nodules.
- A lake subfacies of largely green to gray siltstone and micritic limestone.
- A northern subfacies typified by a) trough cross-bedded channel sandstone b) primarily gray and green siltstone and shale with some red layers, and c) well developed, thick limestone lenses.
- An upper subfacies of calcrete, siltstone, and thin channel sandstone lenses.

Eggs sampled for this study occurred at Egg Mountain (TM-006) within the lake subfacies (Lorenz & Gavin, 1984). The nesting trace (MOR 3062), however, comes from the Flaming Cliffs (TM-160); although unconfirmed at this time, this locality likely occurs in the northern subfacies described by Lorenz and Gavin (1984). The Egg Mountain locality consists of silty mudstones interbedded with silty micritic limestone units, surrounded by shale and siltstone outcrops that Lorenz and Gavin (1984) interpret as lacustrine in origin. Although the Willow Creek anticline resulted from folding and faulting, Lorenz and Gavin (1984) report that shale and siltstone immediately surrounding Egg Mountain are relatively undisturbed. The Flaming Cliffs locality (TM-160) is less than a mile north of Egg Mountain and consists of a calcareous succession of thick silty mudstones, mudstones, and thick, well-developed, silty limestone horizons (personal observation).

Continuoolithus canadensis eggs in this study, as well as the MOR 3062 nesting trace, both come from the WCA 12 miles west of Choteau, Montana. Horner (1987, 1997, 2000) described clutches and isolated eggs from the Egg Mountain locality (TM-

006) in the Upper Cretaceous (Campanian) Two Medicine Formation of Montana. These eggs were later assigned to *Continuoolithus canadensis* (Zelenitsky et al., 1996). One egg contained a poorly ossified and unidentifiable embryo. Horner's (1987, 1997) description includes the egg ornamentation and the typical arrangement of eggs in pairs or linear rows. Hirsch and Quinn (1990) provide the first detailed description of these eggs and eggshells from the Willow Creek anticline locality. Their study includes measurements of egg length and breadth, description of eggshell microstructure, pore morphology, and surface ornamentation. Hirsch and Quinn (1990) assign these eggs to the parataxonomic categories Ornithoid Basic Type and Ratite Morphotype, categories that include avian and non-avian theropod egg types (Mikhailov et al., 1996). Zelenitsky et al. (1996) describe similar eggshell fragments from the temporal and stratigraphically equivalent Oldman Formation of southern Alberta, Canada and assigned this fossil material to the new oospecies *Continuoolithus canadensis* within Incertae sedis. In addition, Jackson and Varricchio (2010) tentatively referred eggshells from the lowermost Two Medicine Formation, exposed at the Sevenmile Hill locality south of Choteau, Montana, to *C. canadensis.*

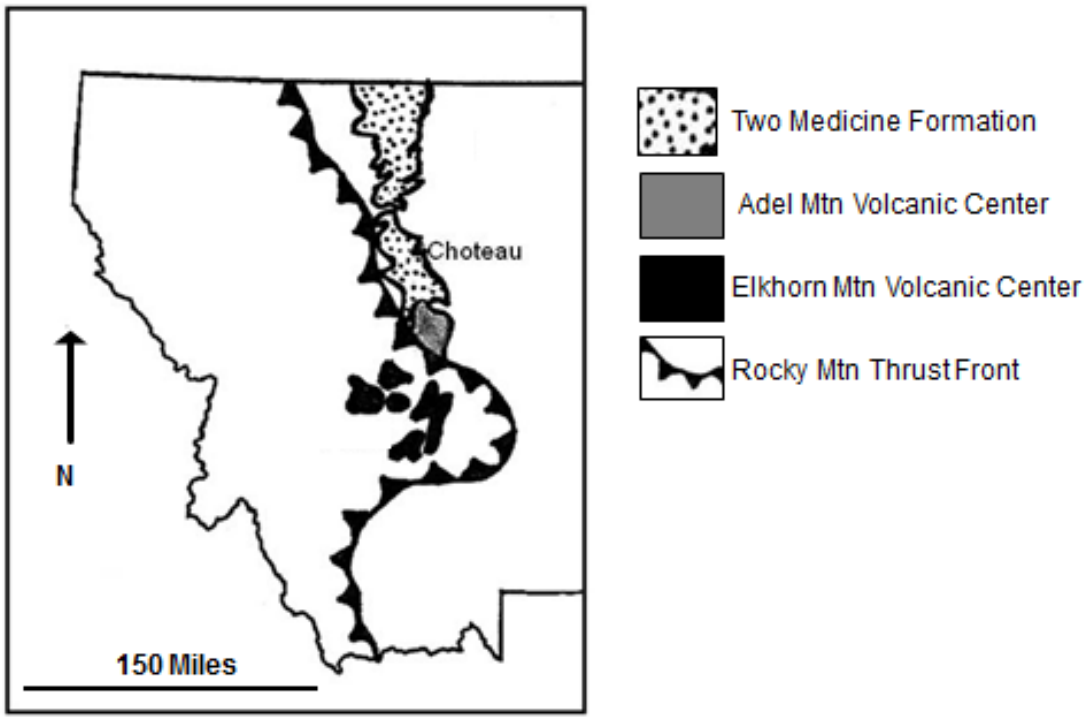


Figure 2. The tectonic setting of western Montana in the Cretaceous. Tectonic map modified from Roberts and Hendrix (2000).

METHODS

Nesting Trace

In 1994, the Museum of the Rockies field school participants collected a *Continuoolithus canadensis* eggshell concentration from the Flaming Cliffs locality (Fig. 3). This eggshell occurred within a green mudstone lens that provided marked contrast to the surrounding red mudstone. At that time the lens and surrounding mudstone were photographed and a field sketch was made of this site showing the relationship of the lens to an overlying carbonate horizon. The following year (1995), additional material was discovered and collected from the same locality. Throughout this study, I refer to this lens containing fossil eggshell as a nesting trace (MOR 3062).

Preparation of Nesting Trace

The nesting trace and fossil material were prepared using a dental pick and small brushes. Oriented rock samples (Table 1) were removed from the specimen for analysis, as described below:

- Mudstone (MOR 3062-S-F1) surrounding eggs and shell fragments at the base of the nesting trace.
- Mudstone (MOR 3062-S-O) that directly overlies the eggshell concentration and contains a band of dark organic matter.
- Mottled mudstone (MOR 3062-S-F2) from within the upper portion of the trace.

- Mudstone (MOR 3062-S-U3) that was truncated by and occurred adjacent to the nesting trace.
- Nodules (MOR 3062-S-N) from within the mudstone surrounding the trace.

These mudstone samples were divided so that a portion of each could be used for various analytical procedures, as described below. Changes in mudstone appearance and texture were documented and photographed from an exposed cross section of the nesting trace (Fig. 5); a cross section was drawn through the center of the specimen (Fig. 4).

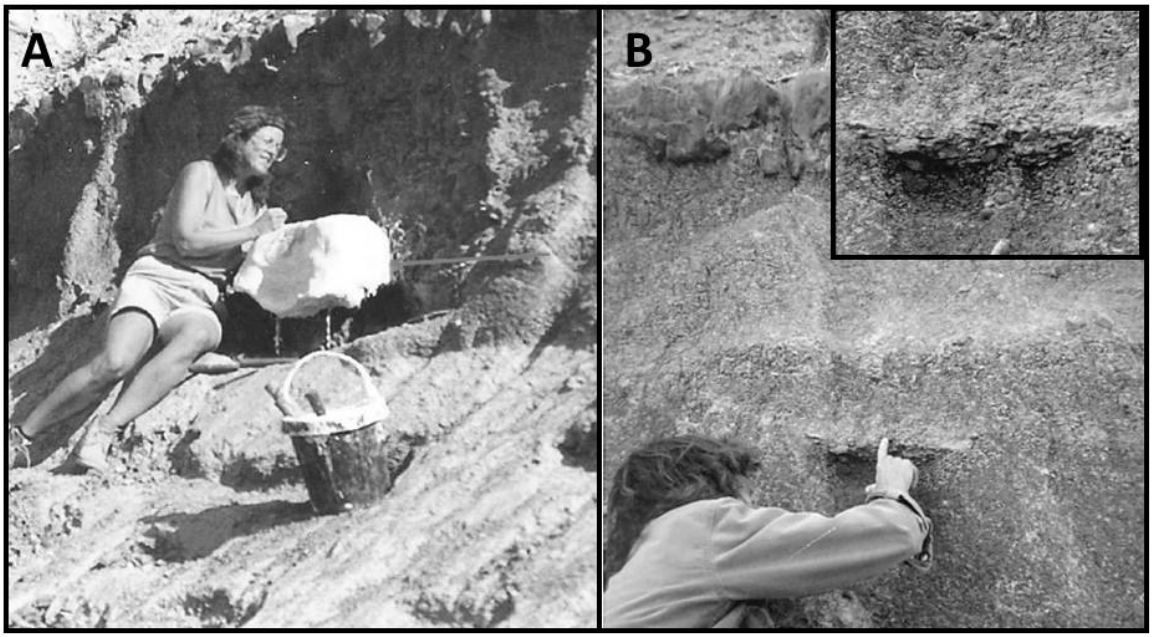


Figure 3. MOR 3062 nesting trace. A) Initial excavation of the trace in 1994. B) Portion of the MOR 3062 trace weathering out of red mudstone. C) Inset photo shows enlargement of the eroding lens containing abundant eggshell fragments. F. Jackson for scale.

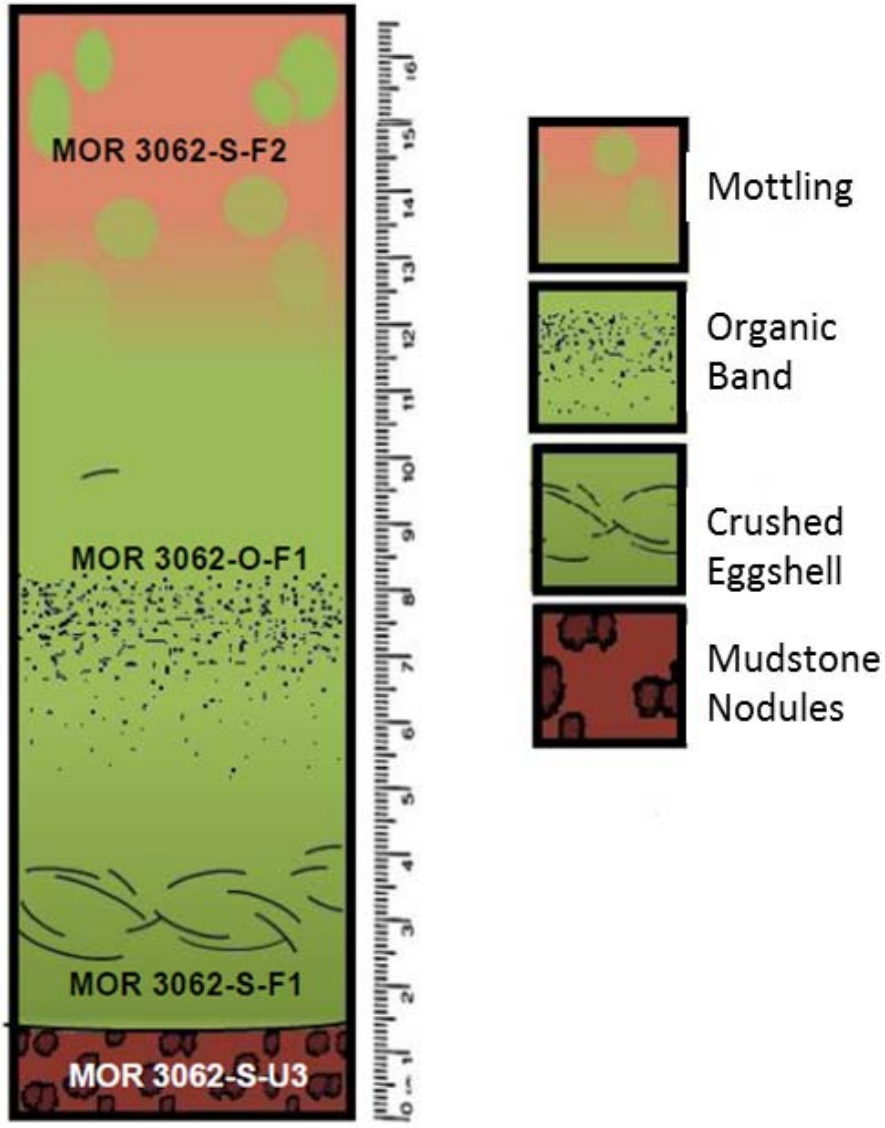


Figure 4. Cross sectional drawing through the center of the MOR 3062 nesting trace. Labels in figure indicate location of sediment sample collection.

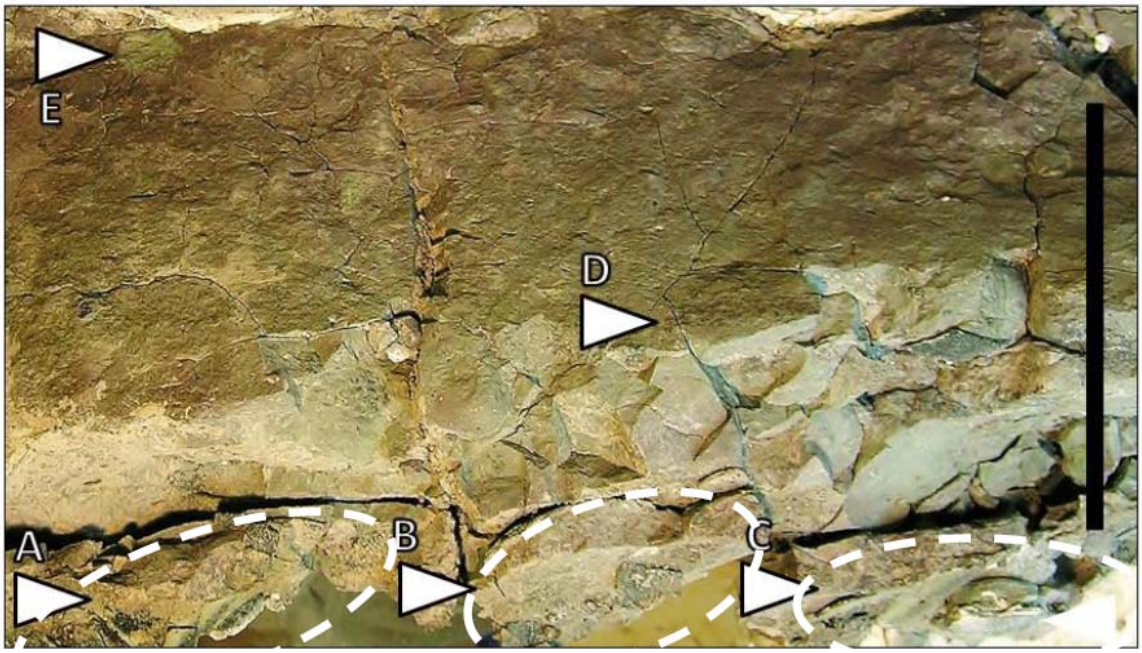


Figure 5. MOR 3062 nesting trace in cross-section showing three compressed eggs indicated by dotted lines (A-C). D) Band of black organic material. E) Mottling at the interface of green and pale red mudstone at the top of the trace. Scale measures 10 cm.

Thin Sections

Thin sections (30 µm thick) were made of eight sediment samples removed from locations within and adjacent to the nesting trace. These included MOR3062-S-F1, MOR3062-S-F2, MOR3062-S-U3, MOR3062-S-O(1), MOR3062-S-O(2), MOR3062-S-O(3), MOR3062-S-N(1), and MOR3062-S-N(2). Half of each slide was stained with Alizarin Red-S and potassium ferrocyanide in order to test for ferroan calcite and ferrous iron content. All slides were examined using a Nikon DS-L1-2M microscope with attached digital camera. Each thin section was photographed at various magnifications (2x, 10x, and 20x) and images imported into *ImageJ* software for analysis.

Total Organic Carbon

Three samples were tested for total organic carbon (TOC): MOR 3062-S-F1, MOR 3062-S-U3, and MOR 3062-S-O. These samples were processed by National Petrographic Services Inc. Houston, Texas; a LECO CR-412 carbon analyzer was used to process dried and acidified sediments. Dried sediment was used to generate a percent mass for total carbon, whereas acidified sediment was used to determine the percent mass for organic carbon. All sediment was combusted in an oxygen atmosphere and carbon present converted to CO^2. A non-dispersive infrared (NDIR) detection cell allowed measurement of the mass of CO^2 present, and this value was then converted to percent carbon based on dry sample weight. Total organic carbon content was subtracted from the total carbon content to calculate the total inorganic carbon content within the various samples.

X-Ray Diffraction (XRD)

X-ray powder diffraction (XRD) was used to determine mineral content of bulk mudstone samples. The limitations of XRD analysis in the present study include the inability to identify amorphous materials such as the organic matter within the nesting trace. In addition, a mineral must comprise 1 wt% of the sample (or greater) for detection. Mineral phase identification was accomplished using XRD. Mudstone samples (MOR 3062-S-F1, MOR 3062-S-N, and MOR 3062-S-U3) were broken into <1 cm pieces and ground with a mortar and pestle until particles passed through a 325 mesh sieve (45 μm). The powder was then affixed, in random orientation, to a glass slide.

Analyses were performed with a Scintag X1 X-ray diffractometer in a 0-0 configuration. Samples were x-rayed between the angles of 3° and 75° two theta, using copper K alpha radiation at a scanning rate of 4°/min, with a continuous scan and step size of 0.02. Methods of preparation and data collection for XRD were modified from Moore and Reynolds (1989). Additionally, samples MOR 3062-S-F1 and MOR 3062-S-N were prepared for clay mineral identification. This included three separate treatments: glycolation of a powdered sample with ethylene; baking of a powdered sample to 400° C; and preparation of an oriented, air-dried grain mount. Glycolation can change the D-spacing between atomic planes allowing for identification of certain minerals. Baking to a specific temperature can also cause a change in D-spacing, diagnostic for the presence of clay minerals. Oriented samples isolate prominent mineral axes expressed as higher intensity peaks. Scans of the different clay identification treatments were run for 3°-30°. MOR 3062-S-O was not analyzed using XRD because bulk analysis cannot reliably determine organic carbon content and presence of organic matter differentiated this sample from MOR 3062-S-F1. A database of ASTM powder diffraction files was used to compare location and intensity of MOR 3062 mudstone spectra peaks to peaks of known minerals.

Energy Dispersive Spectroscopy (EDS)

Mineral phases were analyzed using energy dispersive spectrometry (EDS). This analysis was used in conjunction with XRD because the detection limit for EDS (~0.1 wt%) is more accurate than that of XRD (~1 wt%). Mudstone samples (MOR 3062-S-

F1, MOR 3062-S-N, MOR 3062-S-O, and MOR 3062-S-U3) of about 1 cm in length were affixed to mounts with double sided carbon tape. Samples were coated with iridium for 30 seconds to reduce charging. A JEOL 6100 scanning electron microscope (SEM) produced x-ray spectra at a 20 kV setting, an aperture setting of 2, and adjusted probe current producing a dead time of 23%. Energy dispersive spectra were gathered, using *Winshell* software. Graphs showing the elemental peaks in each sample were compared and analyzed.

Rock Slabs

Mudstone samples (MOR 3062-S-N, MOR 3062-S-F1,2, and MOR 3062-S-O, MOR 3062-S-U3) were carefully hand ground, using a 7 μm grit and then photographed with a Canon 5D Mark II digital SLR camera. Images were imported into *ImageJ* software for analysis.

Eggs and Clutches

Samples in this study include six relatively complete *Continuoolithus canadensis* eggs: MOR 301B, YPM-PU 22544, MOR 326A, MOR 326B, MOR 326C, MOR 3062A (Table 1; Fig. 6A-F). Five eggs came from the Egg Mountain locality (TM-006; Fig. 6A-E) and one from the nesting trace (MOR 3062A) at the Flaming Cliffs site (TM-160; Fig. 6F). The preserved portions of the eggs vary (Table 2). MOR 301B lacks the tip of the tapering pole, whereas MOR 326B has a fragmentary wide pole, and MOR 326C lacks the base of the wide pole. MOR 3062A has a three dimensional side that comprises the

tapering pole, equator and wide pole; however, the reverse side is fragmentary and laterally compressed. MOR 326A has a fragmentary wide pole and shows slight lateral Compression, and YPM-PU 22544 remains intact but highly laterally compressed. Of the five eggs from Egg Mountain, three eggs comprise a partial clutch (MOR 326; Fig. 6C-E). One specimen, YPM-PU 22544, represents an isolated egg (Fig. 6B). MOR 301B (Fig. 6A) occurred in close association with MOR 301A, a relatively uncompressed, intact egg. MOR 301A was not available for study and therefore measurements were obtained from a cast (Fig. 7A). The egg from the Flaming Cliffs (MOR 3062A; Fig. 6F) is relatively complete but compressed. Other eggs and egg portions from the nesting trace were too poorly consolidated and highly compacted to provide useful measurements and are therefore excluded from the study. All six eggs sampled in this study show some degree of lithostatic compression. Therefore egg length and breadth, used in calculation of volume, are based on the cast of MOR 301A, which measures 120 mm long by 55 mm wide. Calipers were used to determine the maximum length and breadth of the eggs. All specimens are cataloged at the Museum of the Rockies, Montana State University, Bozeman, Montana.

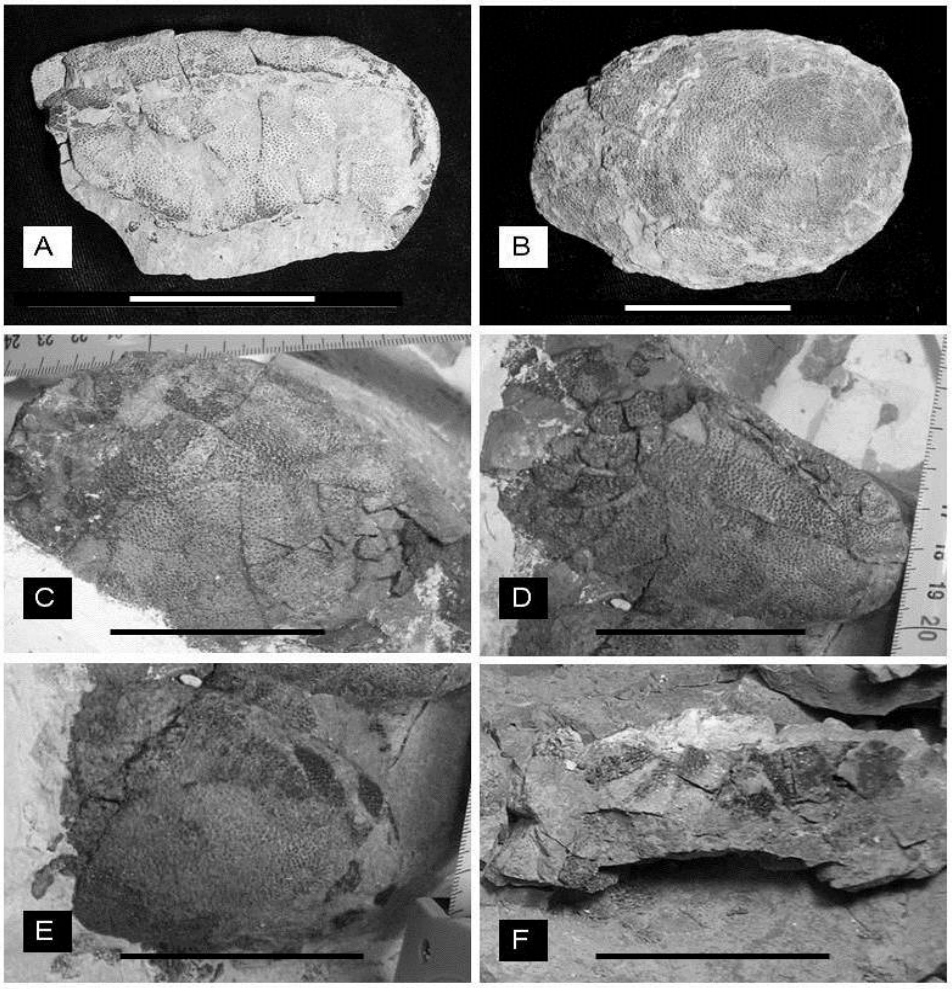


Figure 6. *Continuoolithus canadensis* eggs. A) MOR 301B; B) YPU-PU 22544; C) MOR 326A; D) MOR 326B; E) MOR 326C; F) MOR 3062. Photographs C-E are eggs from the same clutch. All scale bars equal 5 cm.

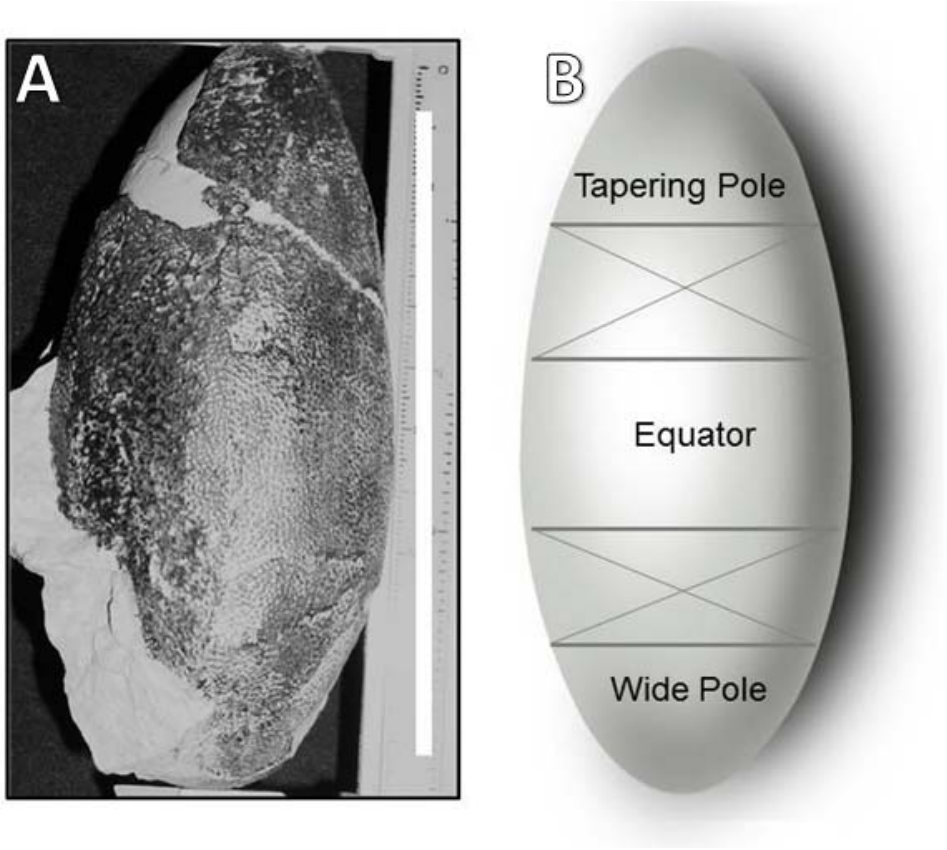


Figure 7. A) Cast of MOR 301A, a relatively un-deformed *Continuoolithus canadensis* egg. Scale equals 10 cm. B) Stylized diagram of an egg showing sampling regions.

Eggshell Preparation

Two eggshell fragments were removed from three regions on each of the six eggs: the tapering pole, the equator, and the wide pole (Fig. 7B). For the two polar regions, samples were taken as close to the poles as possible. For the equatorial region, samples were removed from the centermost location. One fragment from each location was broken and used for radial and tangential thin sections for calculation of water vapor

conductance (GH2O), whereas a second fragment was studied by scanning electron microscopy.

Thin section preparation techniques were modified from Quinn (1994). Eggshells were ultrasonically cleaned and embedded in *Silmar 41* epoxy. The embedded samples were cut in half on a Buhler Isomet saw and prepared as radial and tangential thin sections, ~30 μm thick. Slides were annotated with MOR specimen numbers, a letter indicating region of the egg sampled (T= tapering pole, E= equator, W= wide pole), and type of thin section (R= radial, T= tangential).

Eighteen radial thin sections were examined under a Nikon DS-L1-2M microscope, photographed, and images imported into *ImageJ*. The continuous and mammillary layer thicknesses, node heights, and distances between mammillary cones were measured from 119 images. Each pore in tangential sections was numbered and the pore area calculated (Table 3). Because pore identification is often difficult in fossil eggshell because of diagenetic alteration, criteria were established for pore identification. These included examination of pore shape and exclusion of features smaller than 0.002 mm^2. Adjustment of contrast and brightness in *ImageJ* allowed differentiation between secondary mineral fill within pores and the primary calcite of the eggshell. Where pores appeared substantially enlarged due to dissolution, the original pore size was estimated on the basis of well-preserved pores in the same specimen.

Scanning Electron Microscopy

Eggshell samples were mounted on carbon dots attached to aluminum stubs and coated with iridium for 45 seconds. Coated samples were imaged using a JEOL 6100 scanning electron microscope with energy dispersive spectroscopy capabilities. Imaging was preformed between 15 and 20 kV and captured using *MImage* software. Images were imported into *ImageJ* for further measurement of eggshell features (Table 6). Energy dispersive spectra were gathered to assess elemental composition.

Water Vapor Conductance (GH2O)

Egg measurements obtained from a cast of MOR 301A were used to calculate volume, mass, and surface area, using formulas in Table 4. These values allowed assessment of pore density and GH2O (Table 5). For the purpose of calculations, pores are assumed to be circular in shape, with a length equivalent to shell thickness, and uniform diameter throughout the eggshell. This assumption follows methods in other studies reported in the literature, augmented by observation of radial thin sections of eggshells. I assume that the three egg regions sampled have equal surface area and are weighted equally in calculation of GH2O. This assumption may introduce error and therefore GH2O must be regarded as an estimate, as discussed later.

Measurements of shell thickness (L_s) were obtained from radial sections and exclude node height (Table 4) because pores occur between nodes. For each tangential thin section, total area was determined, as well as number of pores and total pore area. This was used to calculate mean individual pore area (Tables 3). Pore density was also

calculated using the equation in Table 4. Mean pore radius and diameter were determined from the mean individual pore area. Pore density and total surface area allowed estimation of the total number of pores per egg (Tables 4, 5). The number of pores per egg (N) and mean individual pore area (A) allowed estimation of the total pore area per egg (A_p, Table 5). Pore area per egg (A_p) and shell thickness (L_s) permit calculation of GH2O (Table 5). Formulas for egg volume, surface area, mean total pore area and GH2O are provided in Table 4.

Water vapor conductance (GH2O) and number of pores per egg (N) are calculated assuming that the surface area remains the same for each region, whereas the pore density varies. Number of pores per egg (N) is calculated by assuming that the density of pores remains the same over the entire surface of each egg, thus GH2O represents an approximation.

To determine the effect of reduction or absence of the mammillary layer on overall shell thickness, GH2O was also calculated using the same variables (Table 4. 5) with an "idealized" mammillary layer thickness added to the continuous layer thickness for an adjusted overall shell thickness. This idealized mammillary thickness (0.15 mm) was based on complete and well-preserved mammillary cones in the tapering pole of MOR 326B.

Standard deviations, *t*-tests, *p*-values, and confidence intervals were calculated for most variables in this study including eggshell thickness, pore area, pore density and GH2O. Standard deviation was calculated with Excel software. All other statistics were calculated using GraphPad software.

DESCRIPTION

Nesting Trace

The nesting trace occurred at the Flaming Cliffs locality, a succession of thick, silty, calcareous, mudstones, calcareous mudstones, and thick, well-developed, silty limestone horizons. The trace displayed a distinct lenticular shape and measured 43 cm wide and approximately 12-16 cm deep. The lens occurred within oxidized mudstone that differed chemically from the trace. Both the trace and the unit it truncated were comprised of uniform mudstones. No evidence of sedimentary structures was noted. Below, I describe a micostratigraphic section through the nesting trace and truncated unit as shown in Figures 4 and 5; rock samples analyzed are indicated by number. Designation of material as organic is based on total organic carbon analysis presented below.

The trace truncated a red-brown mudstone (MOR 3062-S-U3) containing numerous resistant mudstone nodules (MOR 3062-S-N) which range from 2-4 cm in diameter. Nodules exhibited the same color and grain size as the red mudstone and exhibited distinct borders. Rounded in shape, the nodules often comprised several attached parts. Each nodule displayed an internal dendritic pattern when broken, interpreted as rhizolith structures (Fig. 8). The lower portions of the nodules showed crescent-shaped geopetal fabrics of gravitative cement (Fig. 8; Flugel, 2004). The rhizolith traces were darker than the surrounding red mudstone nodule.

The nesting trace, from stratigraphically lower to higher, consisted of the following lithologies and fossil material. A 1.5 cm structureless, green, calcareous mudstone (MOR 3062-S-F1) overlain and truncated a red-brown mudstone, forming the base of the bowl-shaped depression. A 2 cm-thick layer of eggshell fragments, egg portions, and one relatively complete egg occurred immediately above this green mudstone. Most eggshell concentrations retained the three dimensional shape of the original egg, with the long axes parallel to the truncated surface of the depression. These included one egg and portions of three others. The eggs were not in direct contact with each other, displayed little variation in depth and were arranged such that three of the eggs lay with their long axes parallel to one another and the fourth lay with its long axis perpendicular to the first three (Fig. 5). The relatively intact ovoid egg measured 9.86 cm by 3.63 cm. All egg portions exhibited lithostatic compression with superimposed eggshell fragments. Green mudstone filled the eggs and surrounded the shell fragments. Eggshell fragments and egg portions exhibited several orientations within mudstone: concave upward, concave downward, and vertical. Most of the larger egg portions displayed multiple, superimposed eggshell layers within the mudstone that filled the interior (Fig. 9). Only two small scattered eggshells occurred above this shell concentration. A 3.0 cm interval of green mudstone overlaid the eggshell layer; above this shell layer, a thin discontinuous (< 1cm) band of organic matter (MOR 3062-S-O) occurred approximately midway through the trace (Fig. 10A). This horizontal band was restricted to the trace and its greatest thickness occurred over the densest part of the eggshell concentration. The band had a discrete upper surface of dense organic particles

and an irregular lower contact where particles became less dense with depth; spotty organic particles occurred up to 12 mm below the band. Structures present in the organic band included both concentrations of amorphous organic matter and discrete plant material. These features include a 0.3 mm-wide oval with central cavity (Fig. 11 A), a 0.8 mm and a 1.5 mm elongate structure (Fig. 11 B, C), the latter with cell-like structures extending along one side, and many short (< 0.5 mm) sinuous, thin fibers. Above the band, the mudstone graded from green to pale red over a distance of 3.0 mm. The pale red mudstone (MOR 3062-S-2) exhibited green mottles (Fig. 10 B). Mottles adjacent to the dark band had diffuse perimeters, which became discrete higher in the lens.

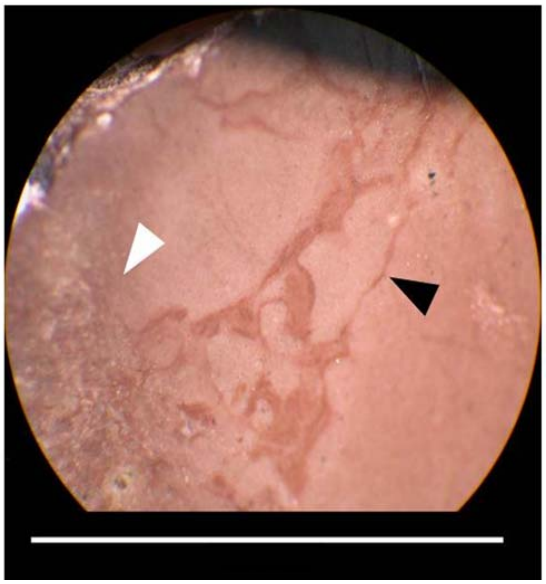


Figure 8. Cross-section of a nodule from within the red mudstone truncated by the MOR 3062 nesting trace. Black arrow indicates rhizolith structure. White arrow indicates gravitative cement along the lower surface of the nodule. Nodule is oriented at an oblique angle. Scale equals 10 mm.

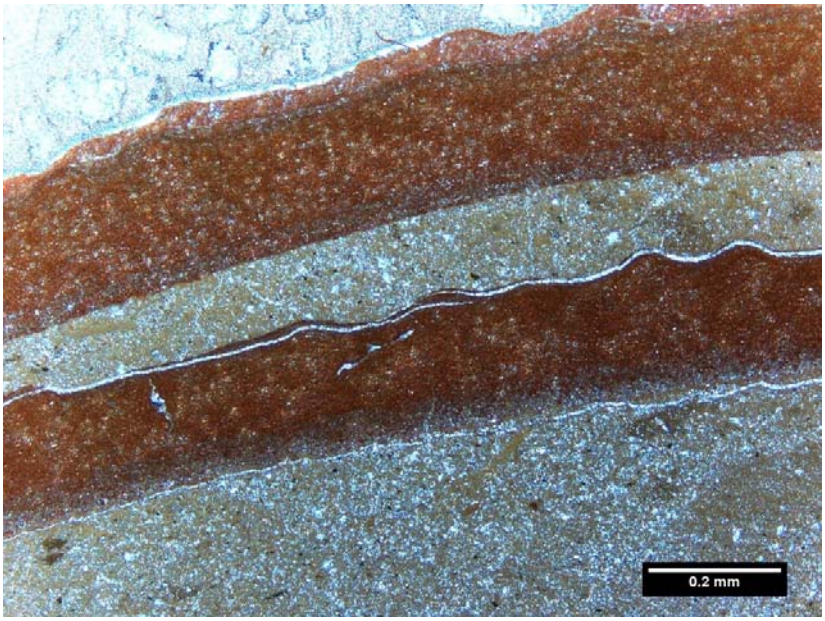


Figure 9. Radial thin section of MOR 3062A eggshell. Eggshell layers are superimposed and separated by mudstone due to lithostatic compaction. Scale measures 0.4 mm.

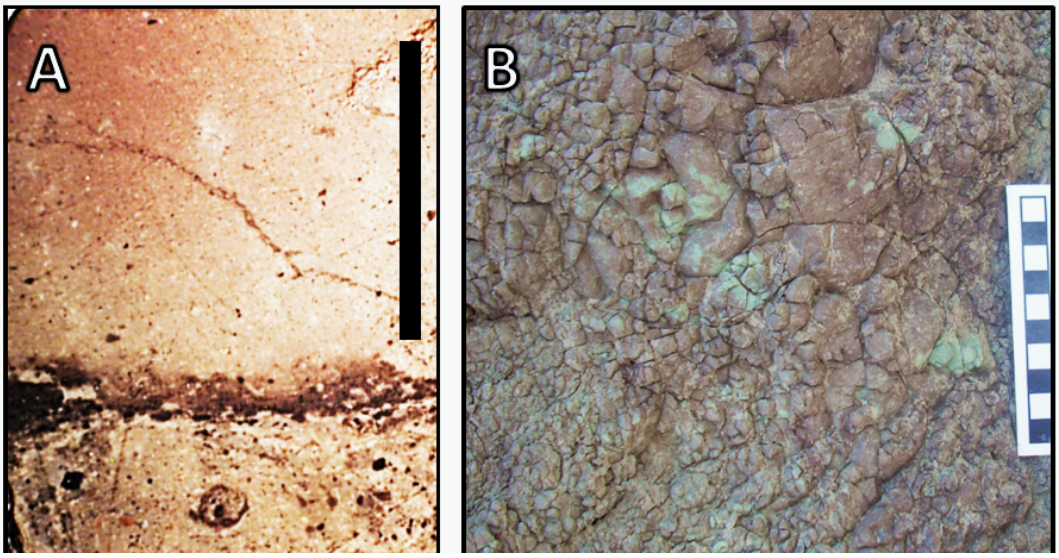


Figure 10. Organic band (MOR 3062-S-O) and pale red, mottled, mudstone (MOR 3062-S-F2). A) Organic band with green mudstone below and pale red mudstone above. B) Mottled mudstone filling the top and overlying the trace and overlying MOR 3062-S-F2. Scale measures 10 mm in A and 10 cm in B.

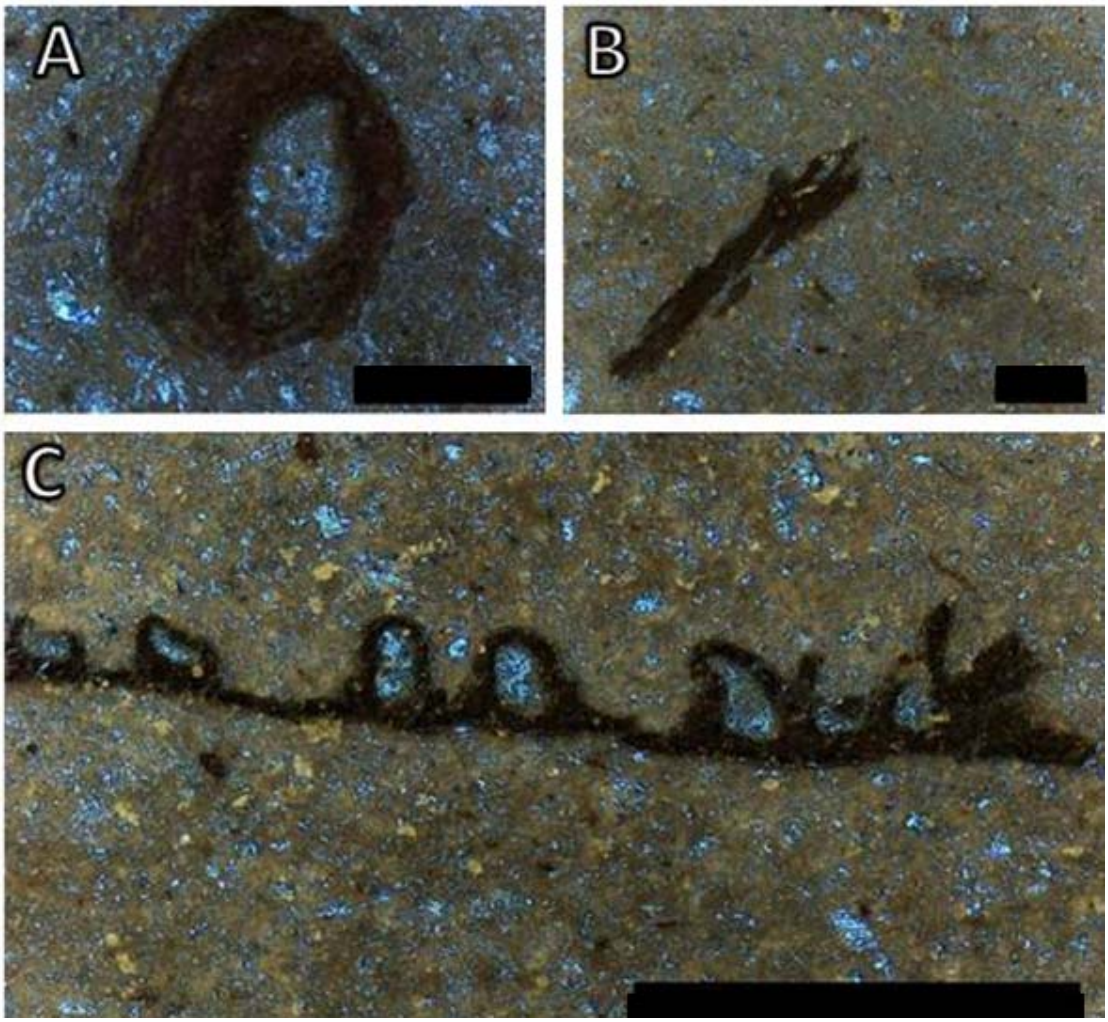


Figure 11. Thin sections of organic material from MOR 3062 nesting trace. A) Cylindrical structure. B) Elongate structure. C) Elongate structure with cell-like structures on one side. Scale measures 0.4 mm for all images.

Total Organic Carbon

Total organic carbon content for each sample was as follows: green mudstone, sampled from immediately below the eggshell concentration (MOR 3062-S-F1) included 0.08% organic carbon with a reaction rating of 2 (on a scale of 1-5), indicating a moderate reaction. Mudstone containing a portion of the dark band (MOR3062-S-O) was

0.06% organic carbon with a reaction rating of 2, whereas the truncated red mudstone (MOR3062-S-U3) consisted of 0.01% organic carbon with a reaction rating of 2 (Table 7).

Iron Staining

Thin sections had varied reactions to the iron stain (Table 7). Red mudstone from the unit truncated by the lens (MOR 3062-S-U3) displayed a substantial amount of oxidized iron in the unstained half of the slide (Fig. 12A, B), whereas staining revealed little additional iron was present. Nodules from within this red mudstone (MOR 3062-S-N) displayed significant oxidization of iron in the unstained half of the slide (Fig. 12 C, D). Staining, however, revealed a significant amount of additional iron that was not oxidized. Rhizoliths, noted in the nodules, were clearly seen in thin section and staining revealed the presence of little iron directly adjacent to these structures. Gravitative cement in these nodules also showed less iron than in adjacent areas. The red mudstone and associated nodules exhibit the same color, texture, and apparent grain size and are nearly indistinguishable in hand sample. The only features that distinguish them from one another are the degree of induration and the amount of non-oxidized iron in the nodules versus the red mudstone. Green mudstone in the lower portion of the lens (MOR 3062-S-F1) displayed essentially no oxidized iron in the unstained portion of the slide (Fig. 13 A, B). However, staining showed a significant amount of iron occurred present in a reduced state (Fig. 13). The organic band (MOR 3062-S-O) displayed some oxidized iron in the unstained portion of the slide; however, this specimen showed about three

times the iron content after staining (Fig. 13 C, D). Fill from the mottled upper portion of the lens (MOR 3062-S-F2) showed some oxidized iron in the unstained portion and nearly twice the iron content (personal estimation) after staining (Fig. 13 E, F). Other than the nodules, all samples had relatively similar amounts of total iron.

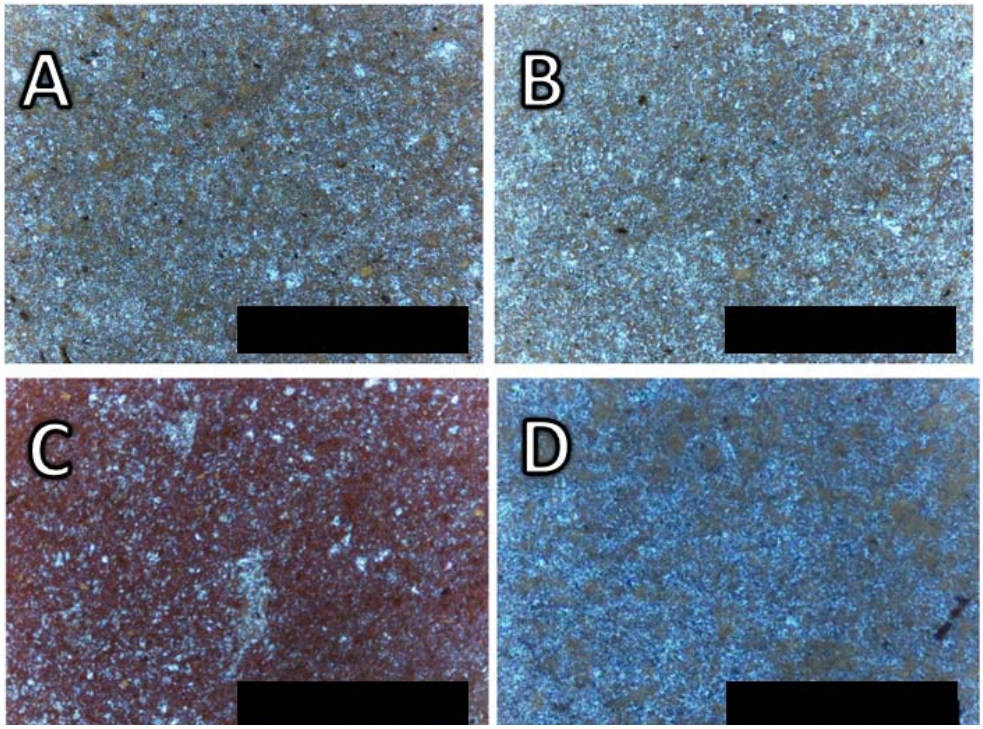


Figure 12. Thin sections of red mudstone (MOR 3062-S-U3) and nodules (MOR 3062-S-N). A) MOR 3062-S-U3 showing iron staining; B) MOR 3062-S-U3 unstained; C) MOR 3062-S-N showing iron staining; D) MOR 3062-S-N unstained. Scale measures 0.4 mm.

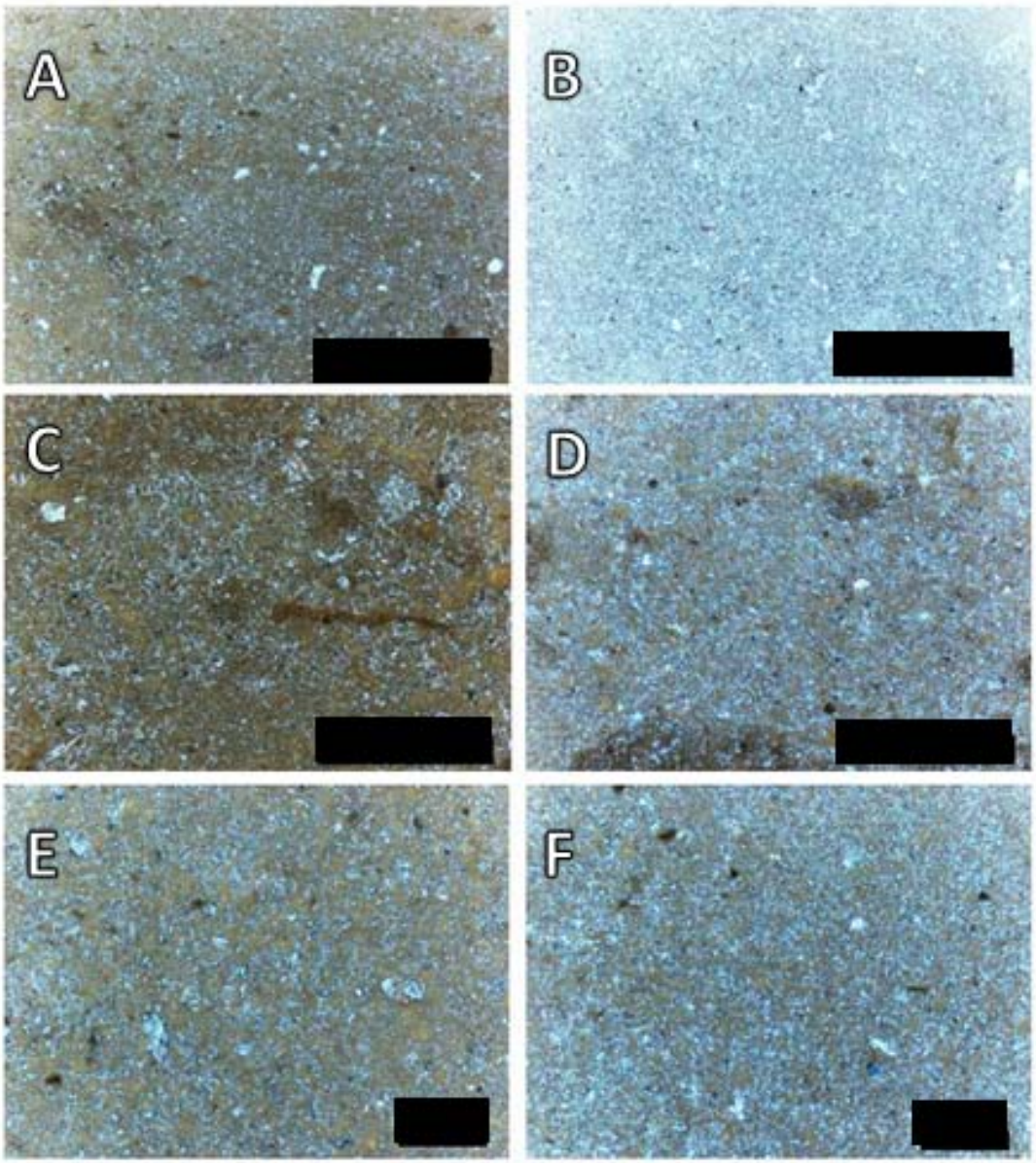


Figure 13. Thin sections of mudstone from within the MOR 3062 nesting trace. A) Fe stained MOR 3062-S-F1. B) Unstained thin section of MOR 3062-S-F1. C) Fe stained thin section of MOR 3062-S-O. D) Unstained thin section of MOR 3062-S-O. E) Fe stained thin section of MOR 3062-S-F2. F) Unstained thin section of MOR 3062-S-F2. Scale is 0.2 mm for all images.

X-Ray Diffraction

X-ray diffraction spectra of mudstone sampled from the base of the nesting trace (MOR 3062-S-F1) was compared to the nodules (MOR 3062-S-N) and the surrounding host rock (MOR 3062-S-U3). All samples are composed almost entirely of quartz, calcite, and albite, listed in order of abundance (Fig. 14). Additionally, a spike at about 9° (present in all samples), indicates a small amount of aluminum silicate, probably muscovite or illite; however, clay treatments failed to confirm this interpretation. X-ray diffraction analysis of the green mudstone from within the nest (MOR 3062-S-F1) revealed a small peak collapse after heat treatment at 12.5°, consistent with sepiolite. The intensity of the peak indicates that this is a minor constituent. Alternatively, it may represent some other magnesium silicate or member of the chlorite group because another peak at ~18° is consistent with chlorite in the sample. X-ray diffraction spectra of the nodules (MOR 3062-S-N) reveal several peaks that are absent from both mudstone within the lens and the host unit. These included a possible gypsum (calcium sulfate) peak at 20°, a possible anhydrite peak at 25°, and additional calcite peaks that exhibit greater intensity than those noted in MOR 3062-S-F1.

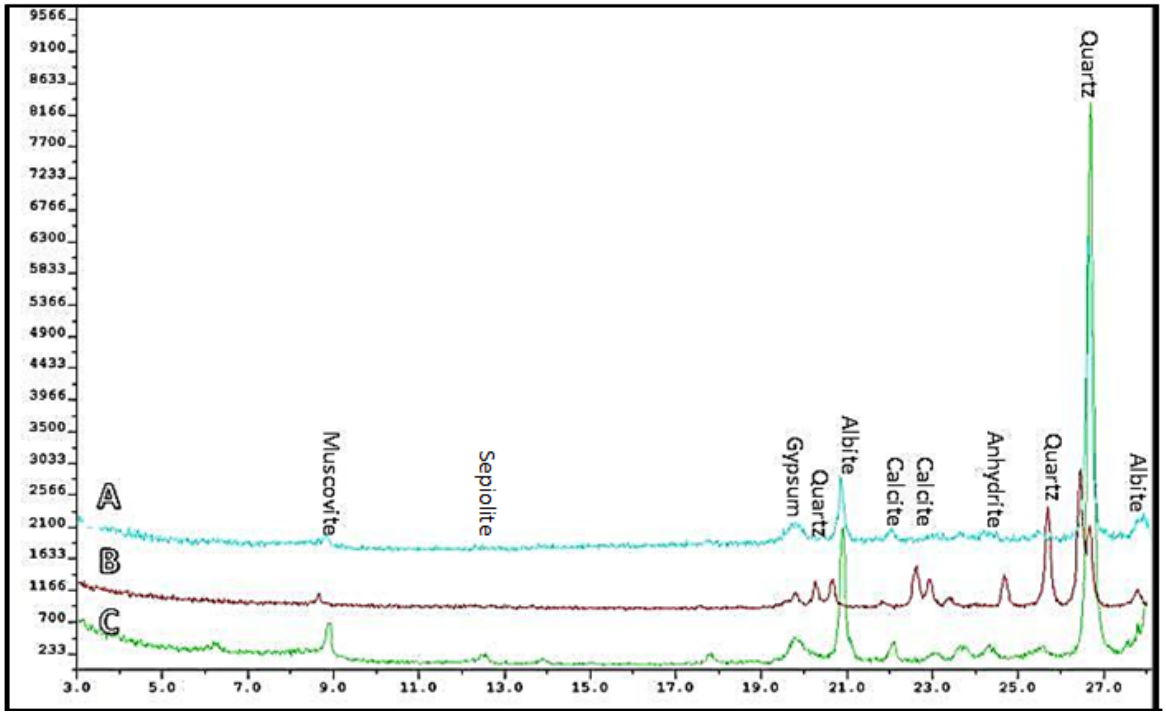


Figure 14. XRD results for mudstones from the Flaming Cliffs Site. A) Red mudstone (MOR 3062-S-U3) truncated by the MOR 3062 nesting trace. B) Nodules from within the red mudstone (MOR 3062-S-N). C) Green mudstone (MOR 3062-S-F1) from the base of the MOR 3062 nest. X-axis is degrees 2 Theta. Y-axis is intensity. Range shown includes 3-30 degrees, the most likely range in which clay mineral would occur.

Energy Dispersive Spectroscopy

Energy dispersive spectra reveal several differences in elemental composition between mudstone filling the base of the nesting trace (MOR 3062-S-F1; Fig. 17), the band of organic matter from within the trace (MOR 3062-S-O; Fig. 18), the truncated host mudstone (MOR 3062-S-U3; Fig. 15), and nodules from within the host mudstone (MOR 3062-S-N; Fig. 16). In the order of abundance, all samples consist primarily of Si, O, Al, K, Mg, Ca, Na, and Fe. Mudstone within the base of the trace (MOR 3062-S-F1) displayed a potassium peak nearly three times the intensity of the organic band (MOR

3062-S-O), the nodules from the truncated red mudstone (MOR 3062-S-N), and the red mudstone (MOR 3062-S-U3). All samples showed a low-intensity carbon peak that is consistent with TOC results. This peak was highest in the mudstone from the base of the trace (MOR 3062-S-F1) and in the rhizolith-bearing nodules (MOR 3062-S-N). Of the four samples associated with the trace, only the nodules (MOR 3062-S-N) contain sulfur. Both the nodules and the host mudstone show the presence of titanium. The various peaks of these two samples are almost identical in intensity.

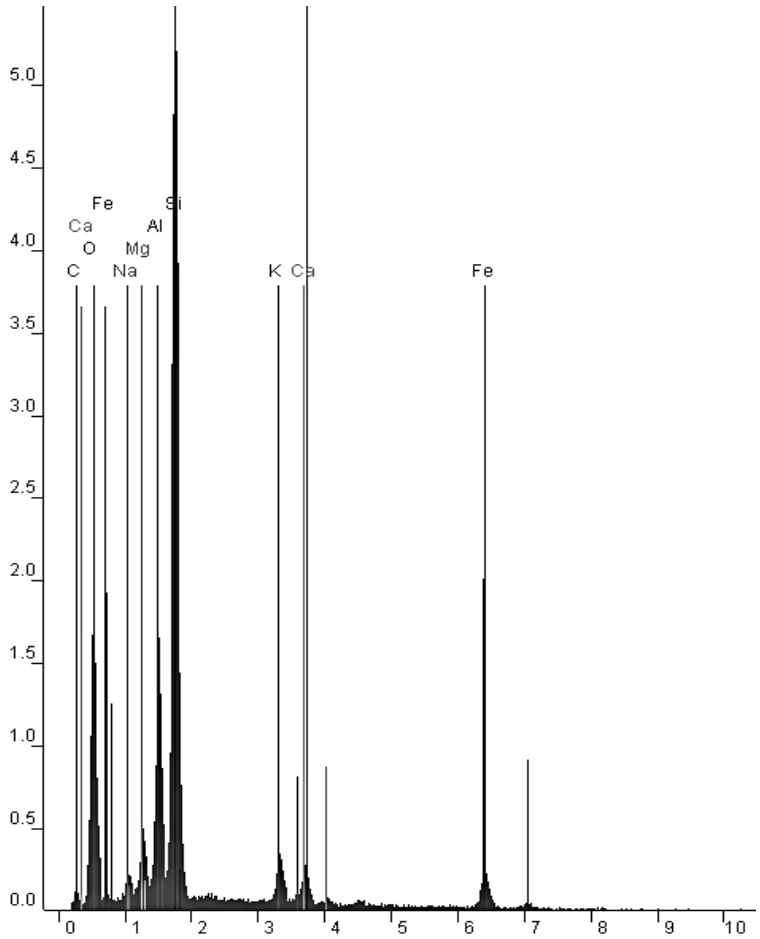


Figure 15. EDS results for red mudstone (MOR 3062-S-U3) truncated by the MOR 3062 nest.

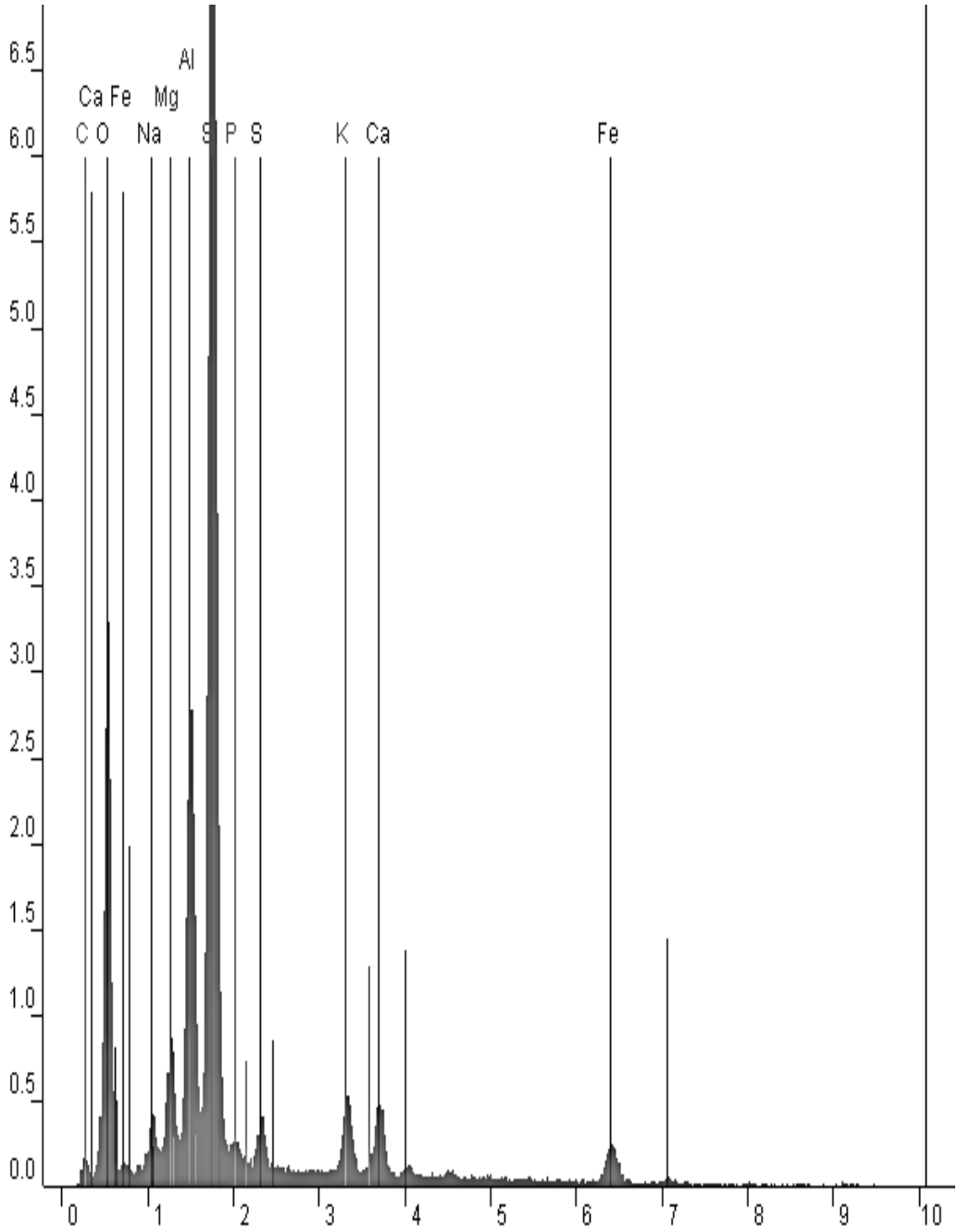


Figure 16. EDS results for nodules in the red mudstone (MOR 3062-S-N). X-axis is KeV. Y-axis is intensity.

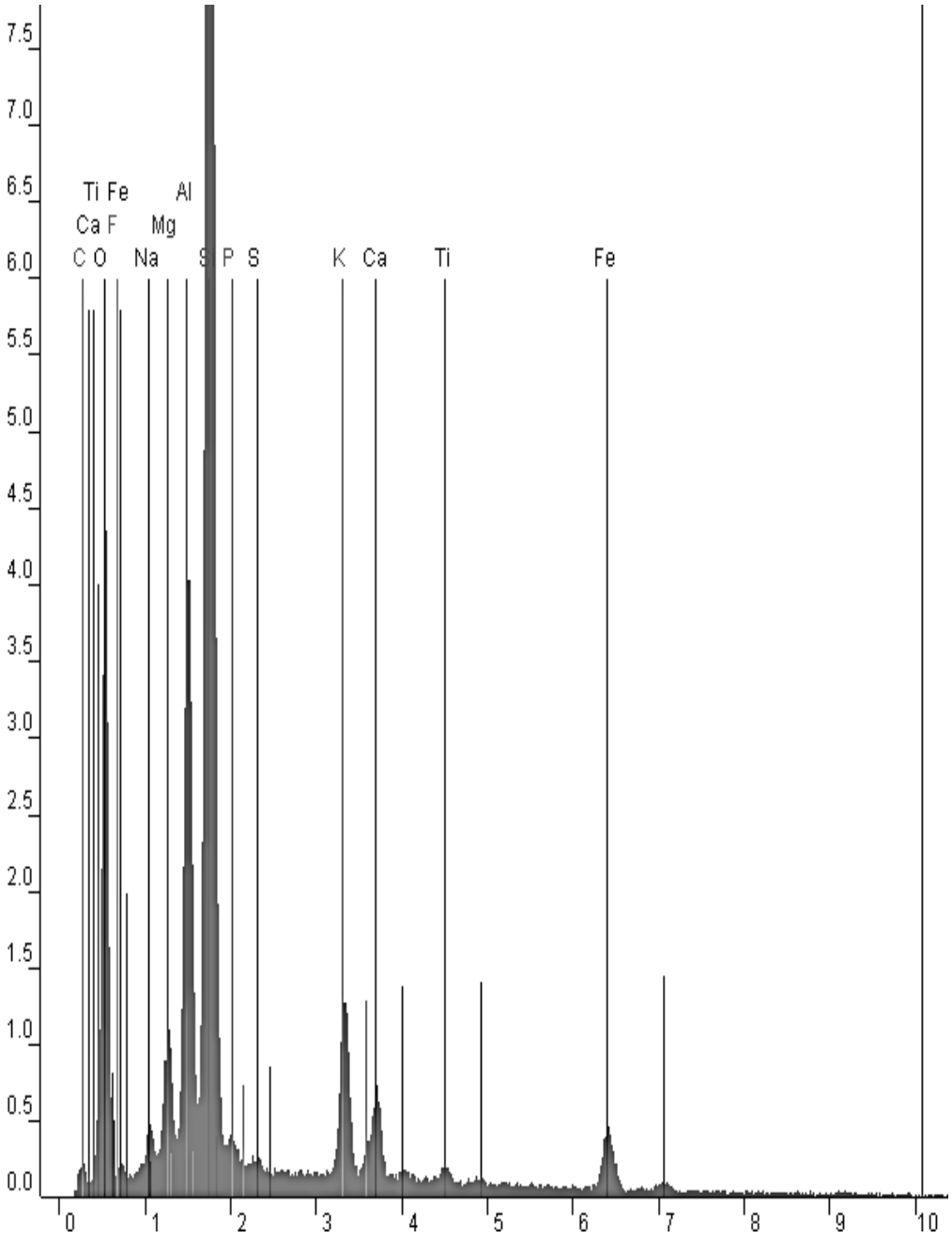


Figure 17. EDS results for the green mudstone (MOR 3062-S-F1) that fills the nest. X-axis is KeV. Y-axis is intensity.

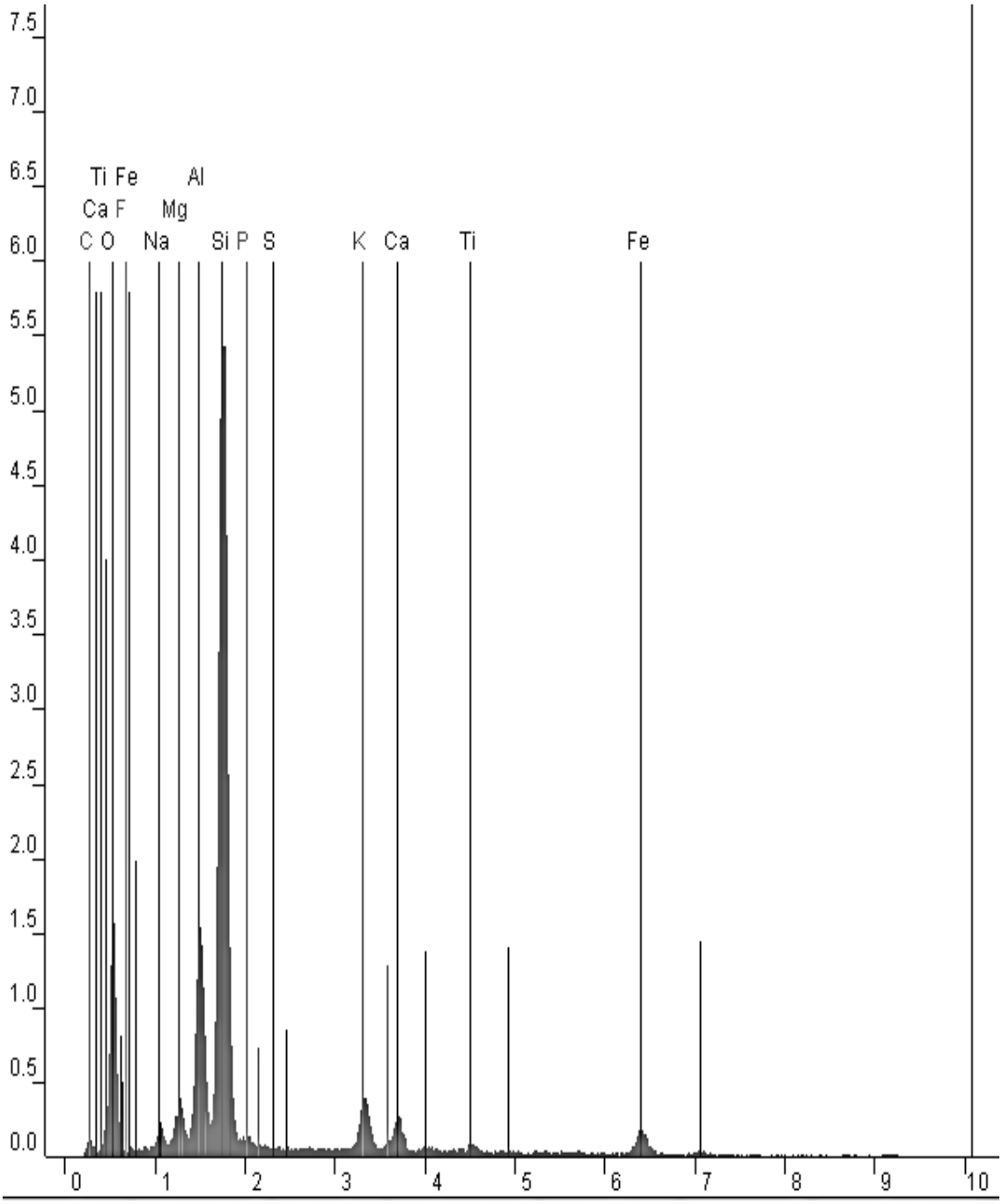


Figure 18. EDS results for the organic band (MOR 3062-S-O) within the nesting trace. X-axis is KeV. Y-axis is intensity.

Eggs and Eggshells

Gross Egg Morphology

Length and breadth measurements for compressed egg specimens are 11.38/7.35 cm (MOR 301B), 11.4/7.98 cm (YPM-PU 22544), 13.91/6.42 cm (MOR 326A), 11.44/5.01 cm (MOR 326B), 6.75/4.75 cm (MOR 326C), and 9.86/3.63 cm (MOR 3062A). However, these measurements include eggs that are incomplete (Table 2). All eggs are oval in shape and appear to have one pole which is wider than the other. Nodes occur at the wide pole and equator for all eggs, with reduced or absent nodes at the tapering poles. Nodes are generally round, occasionally coalesce to form ridges, and vary in height from .01 mm (MOR 3062-T) to 0.23 mm (MOR 326B-E). Original egg volume estimated from MOR 301A (length, 120 mm; breadth, 55 mm), is 185.1 cm^3 (Table 2).

Microstructure

The eggshells exhibit a varying degree of diagenetic and/or biologic alteration and consist of two structural layers of calcite: an inner mammillary layer consisting of cones with radiating calcite spherulites and an outer continuous layer composed of prisms that extend throughout the second layer. The contact between these layers is discrete and regular. Tabular structure (*sensu* Mikhailov, 1997) is visible in both mammillary cones and prisms of the continuous layer (Fig. 19). Squamatic structure and fine horizontal laminations characterize the continuous layer. Eggshell samples from the egg contained within the nesting trace are highly altered; for example, prismatic, squamatic and tabular structures within the continuous layer are poorly preserved. A thin (0.2 mm) deposit of

secondary calcite covers the outer eggshell surfaces, and the mammillary layers are highly reduced or absent. Calcite also fills many pores on the shell's external surface. In two of the six eggs (MOR 301B & MOR 3062A), the mammillary layer is absent from the tapering poles, likely due to dissolution. Because eggshell thickness is used to calculate GH2O, it is important to quantify the effect of dissolution on the mammillary layer. For this reason, thicknesses are reported for 1) all eggshell samples regardless of eggshell completeness, 2) only those eggshell fragments where an intact mammilary layer can be measured, and 3) an idealized sample set using the actual continuous layer thicknesses of the six eggs and assuming a mammillary thickness of 0.15 mm. The value, 0.15 mm, is the maximum mammillary layer thickness observed in the sample set.

Entire Sample Thickness. Regional mammillary layer thickness increases from 0.08 mm at the tapering pole, to 0.10 mm at the equator, to 0.11 mm at the wide pole (Table 4); however, these regional averages also reflect mammillary dissolution. Total shell thickness ranges from 0.65 mm (MOR 3062A, equator) to 1.18 mm (MOR 326B, equator), including ornamentation, and 0.63 mm (YPM-PU 22544, tapering pole) to 1.08 mm (YPM-PU 22544, wide pole) excluding ornamentation (Table 4). Mean shell thickness with standard deviation (SD) across all eggs (excluding nodes) is 0.872 (0.107) mm. Regional mean shell thickness (SD) is 0.833 (0.116) mm at the tapering pole, 0.855 (0.103) mm at the equator, and 0.927(0.094) mm at the wide pole. Regional shell thicknesses for each egg are shown in Figures 20-23. The mammillary layer to

continuous layer thickness ratio varies from 1:4.8 (MOR 326B, tapering pole) to 1:10.5 (MOR 301B, equator) excluding node height (Table 6).

Eggshell Samples with Intact Mammillary Layers. Regional mammillary layer thickness for intact specimens varies from 0.15 mm at the tapering pole, to 0.12 mm at the equator, to 0.11 mm at the wide pole (Table 4). Intact shell thickness ranges from 0.98 mm (MOR 301B, equator) to 1.18 mm (MOR 326B, equator), including ornamentation, and 0.86 mm (MOR 301B, equator) to 0.99 mm (MOR 326C, tapering pole) excluding ornamentation (Table 4). Mean shell thickness (SD) across all eggs (excluding nodes) is 0.914 (0.044) mm. Regional mean shell thickness (SD) is 0.94 (0.078) mm at the tapering pole, 0.90 (0.037) mm at the equator, and 0.92 (0.0; only one sample) mm at the wide pole. The mammillary layer to continuous layer thickness ratio varies from 1:4.87 (MOR 326B, tapering pole) to 1:9.88 (MOR 301B, equator) excluding node height (Table 4).

Thickness of Idealized Sample Set. With an idealized mammillary layer thickness of 0.15 mm, the shell thickness ranges from 0.72 mm (YPM-PU 22544, tapering) to 1.12 mm (YPM-PU 22544, wide pole) excluding ornamentation (Table 4). Mean shell thickness (SD) across all eggs (excluding nodes) is 0.924 (0.096) mm. Regional mean shell thickness (SD) is 0.902 (0.108) mm at the tapering pole, 0.902 (0.091) mm at the equator, and 0.97 (0.091) mm at the wide pole. The mammillary layer to continuous layer thickness ratio varies from 1:3.8 (YPM-PU 22544, tapering pole) to 1:6.5 (YPM-PU 22544, wide pole) excluding node height (Table 4).

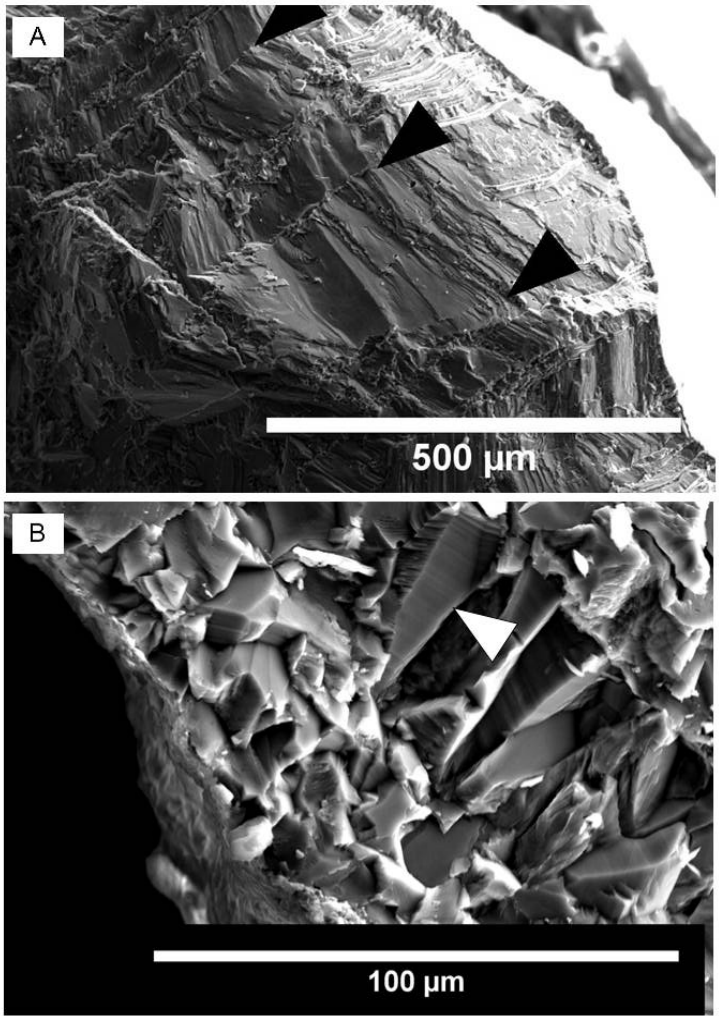


Figure 19. *Continuoolithus canadensis* eggshell. A) SEM of prismatic structure in the continuous layer of MOR 326B. Arrows indicate width of prism; B) single mammillary cone from MOR 326B. Arrow indicates faint calcite laminations.

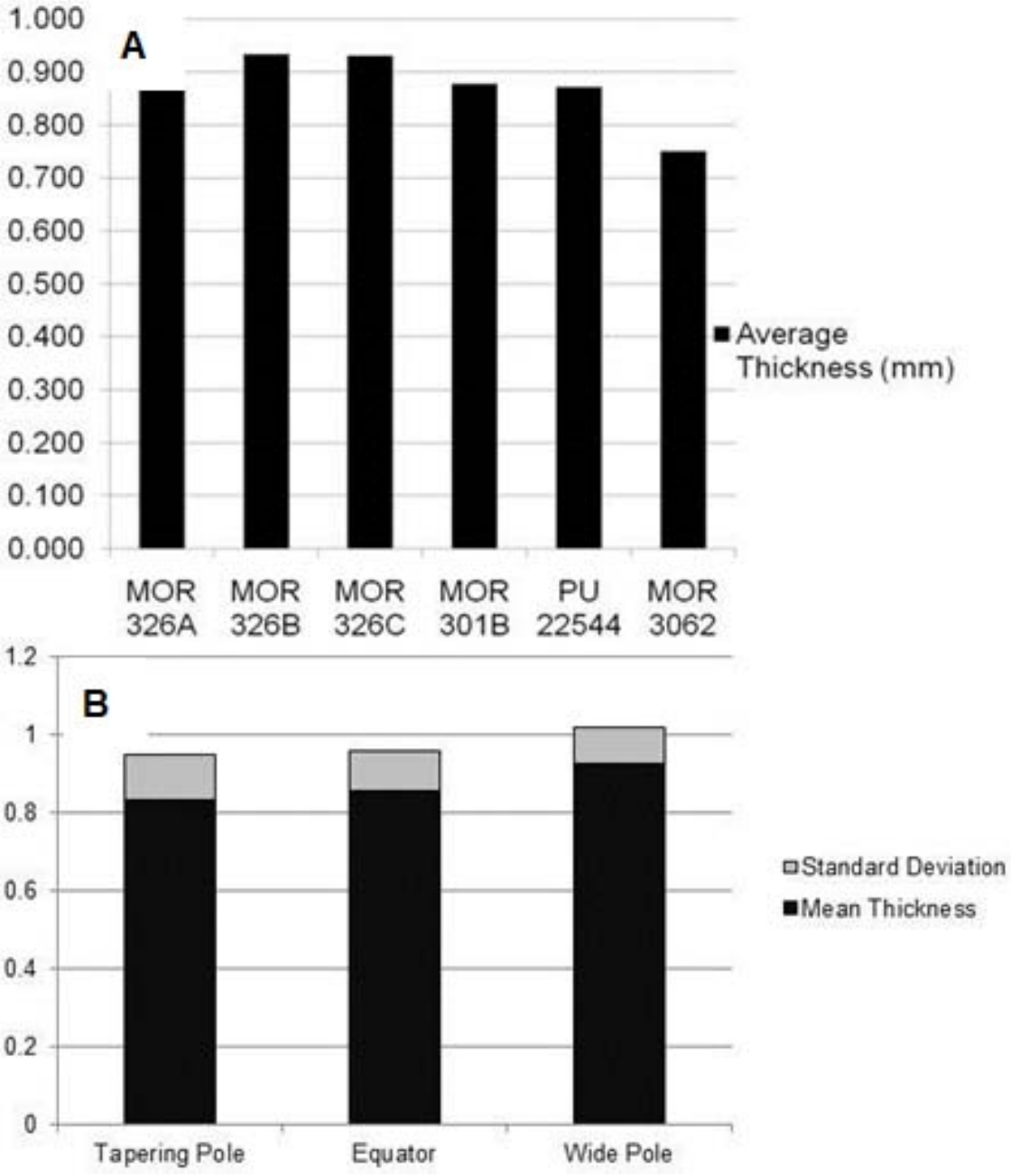


Figure 20. Histograms of eggshell thickness (for entire sample set). A) Average shell thickness across each of six eggs (mean shell thickness for all eggs was 0.87 mm); B) regional mean shell thickness with standard deviation.

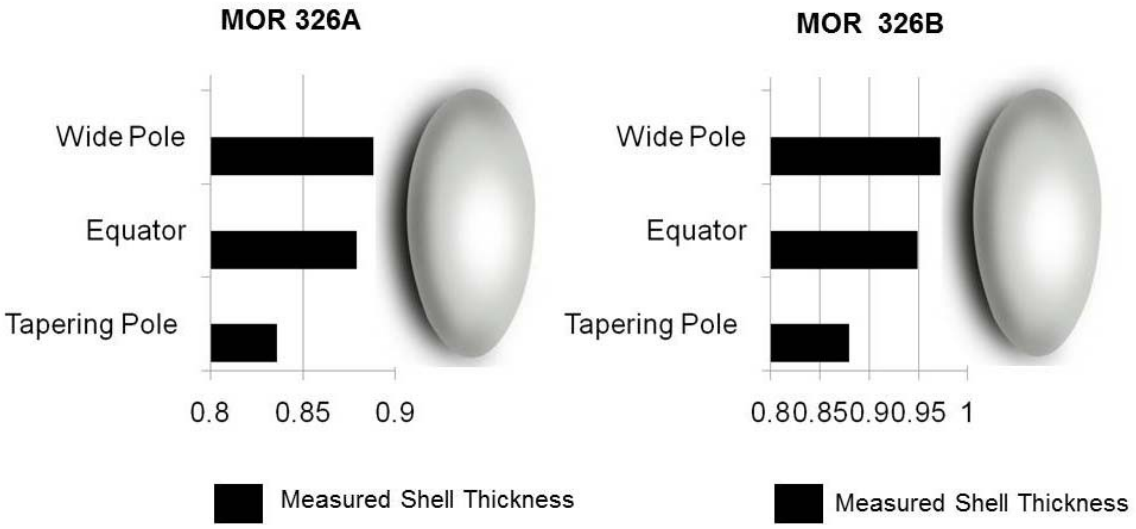


Figure 21. Histogram showing regional shell thickness for MOR 326A and MOR 326B. Histograms are derived from the entire sample set, including samples showing dissolution. X-axis shows thickness in mm. Y-axis shows sampled egg regions.

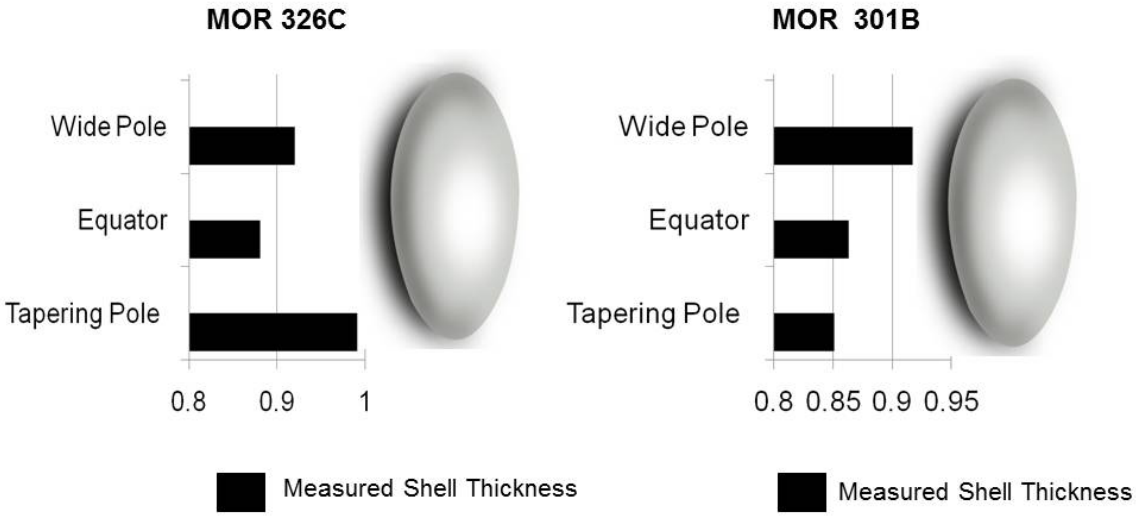


Figure 22. Histogram showing regional shell thickness for MOR 326C and MOR 301B. Histograms are derived from the entire sample set, including samples showing evidence of dissolution. X-axis shows thickness in mm. Y-axis shows sampled egg regions.

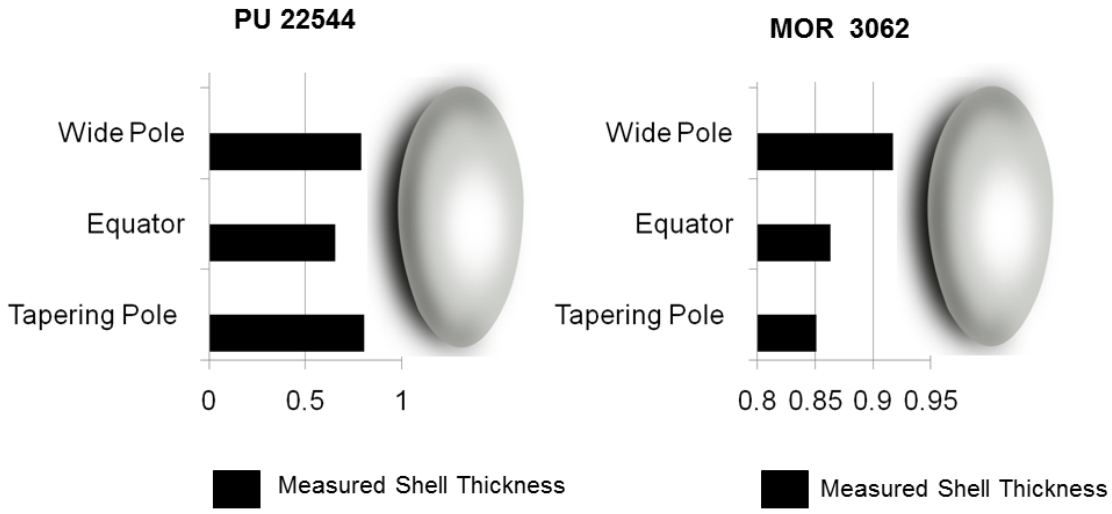


Figure 23. Histogram showing regional shell thickness for YPM-PU and MOR 3062. Histograms are derived from the entire sample set. X-axis shows thickness in mm. Y-axis shows sampled egg regions.

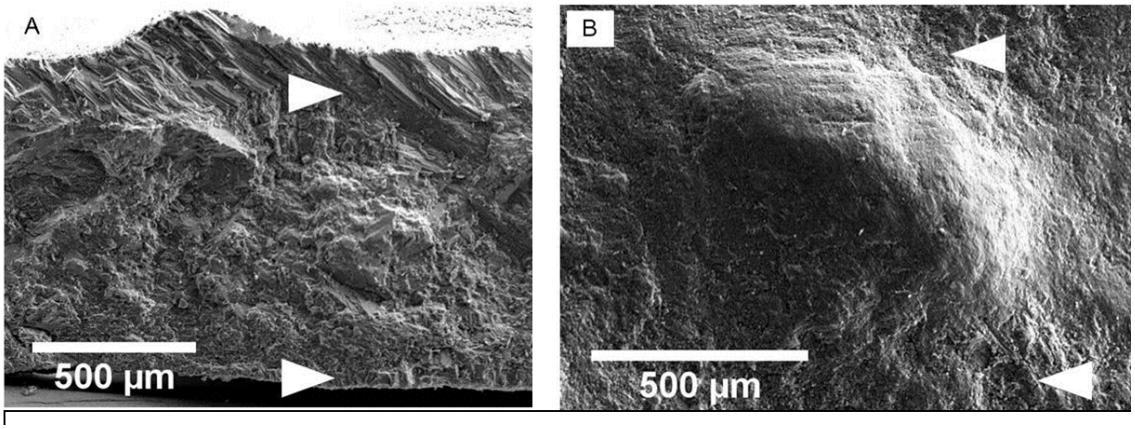


Figure 24. SEM of *Continuoolithus canadensis*. A) Diagenetically altered eggshell, MOR 3062. Arrows indicate secondary calcite and reduced mammillary layer at the outer and inner shell surfaces, respectively. B) Node on the surface of MOR 3062. Arrows indicate matrix-filled pores.

Pore Area and Density

Pore area and density were measured from tangential sections (Table 3). Tangential sections of eggshell varied in total sample area from 5 mm^2 to 34 mm^2. Pores identified in radial thin sections are unbranching and of relatively constant width throughout the shell thickness, consistent with angusticanaliculate pore system (Mikhailov et al., 1996). Pores were typically located on the perimeter of nodes or, to a lesser extent, between nodes. No pores were observed to penetrate nodes (Fig. 24). The following values and ranges for pore area, diameter, and density were measured using data collected from tangential thin sections. Additional data from SEM observation and radial thin sections are included as appropriate (Fig. 25). Mean individual pore area (SD) across all regions of all eggs is 0.007 (0.0024) mm^2. Individual pore areas across all eggs vary from 0.002-0.022 mm^2. All pores photographed under SEM fell within this range. Regional mean individual pore area (SD) is 0.0057 (0.0021) mm^2 for the tapering pole, 0.0071 (0.003) mm^2 for the equator and 0.0082 (0.0016) mm^2 for the wide pole. Mean pore diameter across all regions of all eggs ranged from 0.051 mm to 0.167 mm. A pore in one radial thin section displayed some variability in pore diameter measuring 0.127 mm at the outer surface of the continuous layer, 0.207 mm just below the shell surface, and 0.101 mm at the continuous-mammillary layer boundary. The 0.207 mm diameter falls outside of the range measured from survey of tangential sections and likely results from dissolution. Mean pore density is 0.3 pores per mm^2 at the tapering pole, 0.7 pores per mm^2 at the equator, and 0.4 pores per mm^2 at the wide pole. Pore density across all tangential samples ranged from 0.1 pores per mm^2 to 1.59 pores per mm^2.

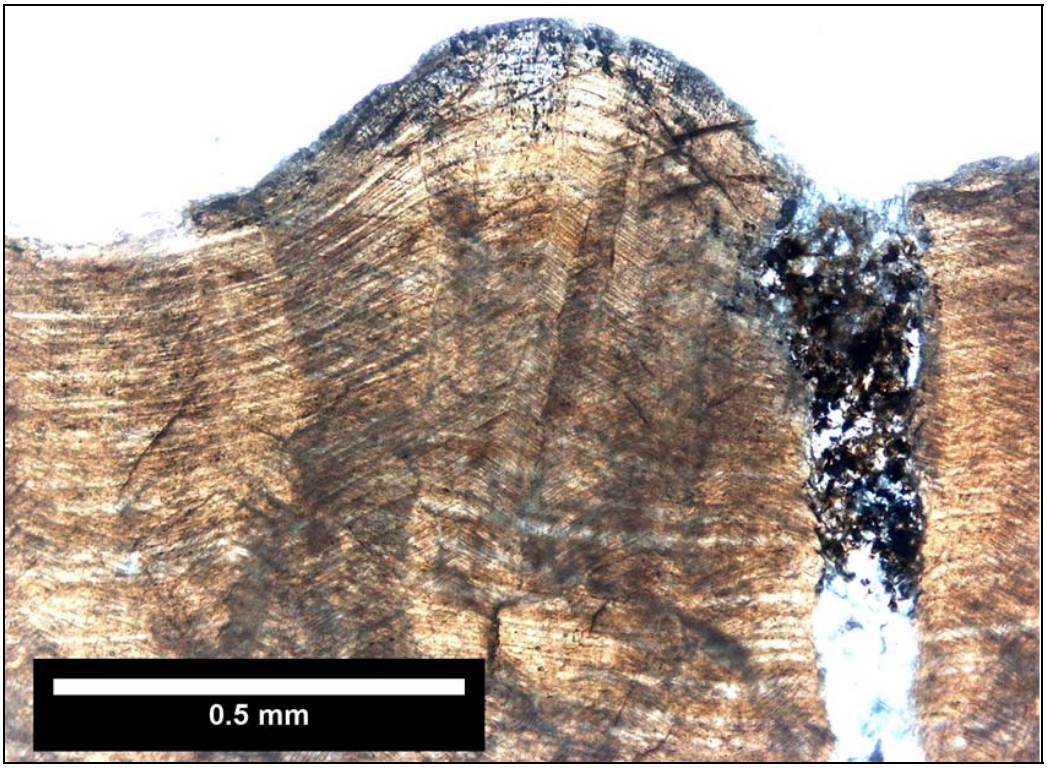


Figure 25. Radial view of MOR 326C showing calcite filled pore and adjacent node.

Water Vapor Conductance

As with eggshell thickness, values of GH2O were calculated for 1) the entire sample, regardless of eggshell completeness; 2) only those eggshell fragments where a complete mammillary layer was measured; and 3) an idealized sample set using the actual continuous layer thicknesses of the six eggs with an idealized mammillary thickness of 0.15 mm. Figures showing the actual condition of the mammillary layer are provided below (Figs. 26-31), and table 8 in the appendix includes the data (Table 8). A histogram shows pore area and density used in GH2O calculation (Fig. 32).

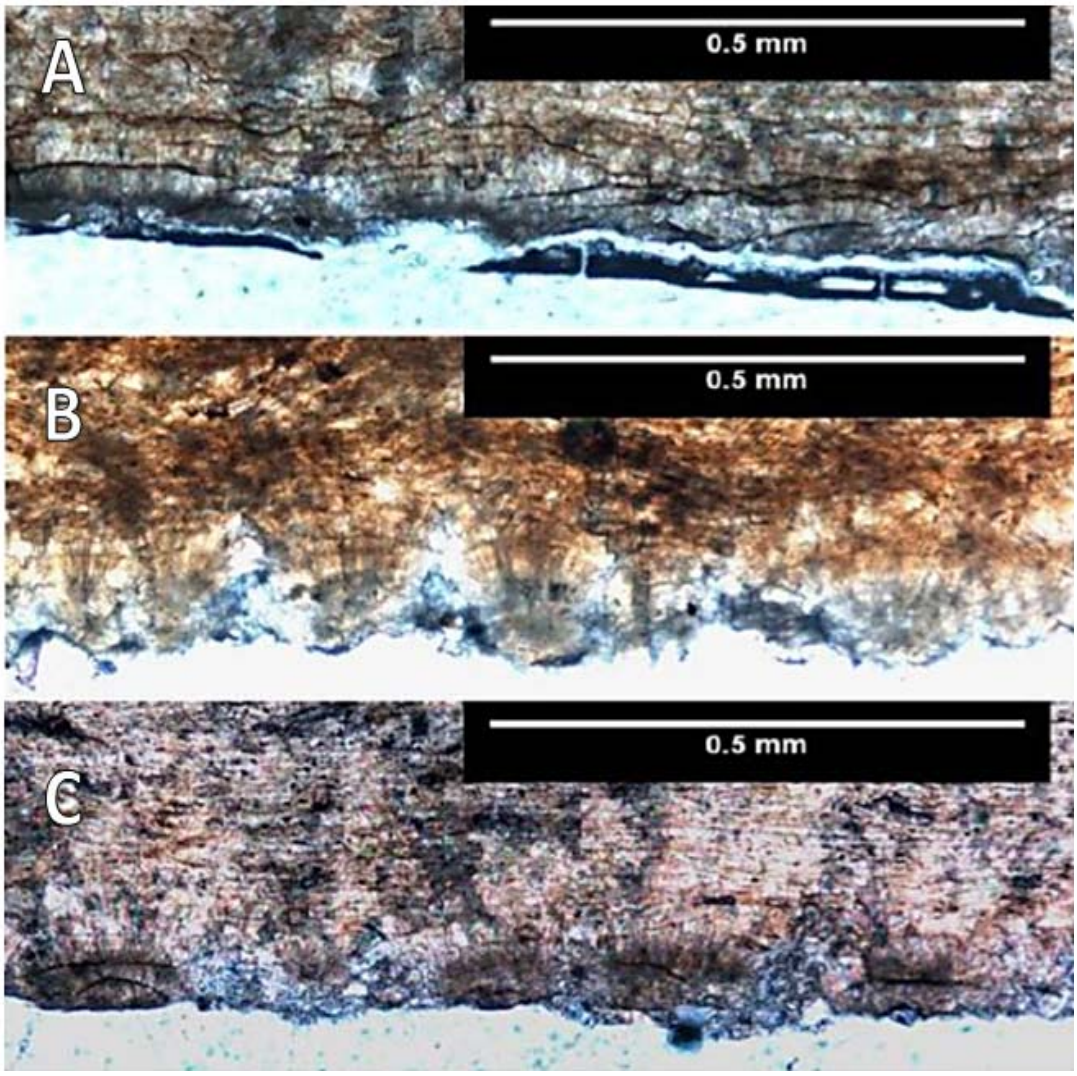


Figure 26. Radial views of MOR 326A. A) Eggshell from wide pole showing reduced mammillary cones. B) Eggshell from equator showing dissolution between cones. C) Eggshell from tapering pole showing mostly complete mammillary cones.

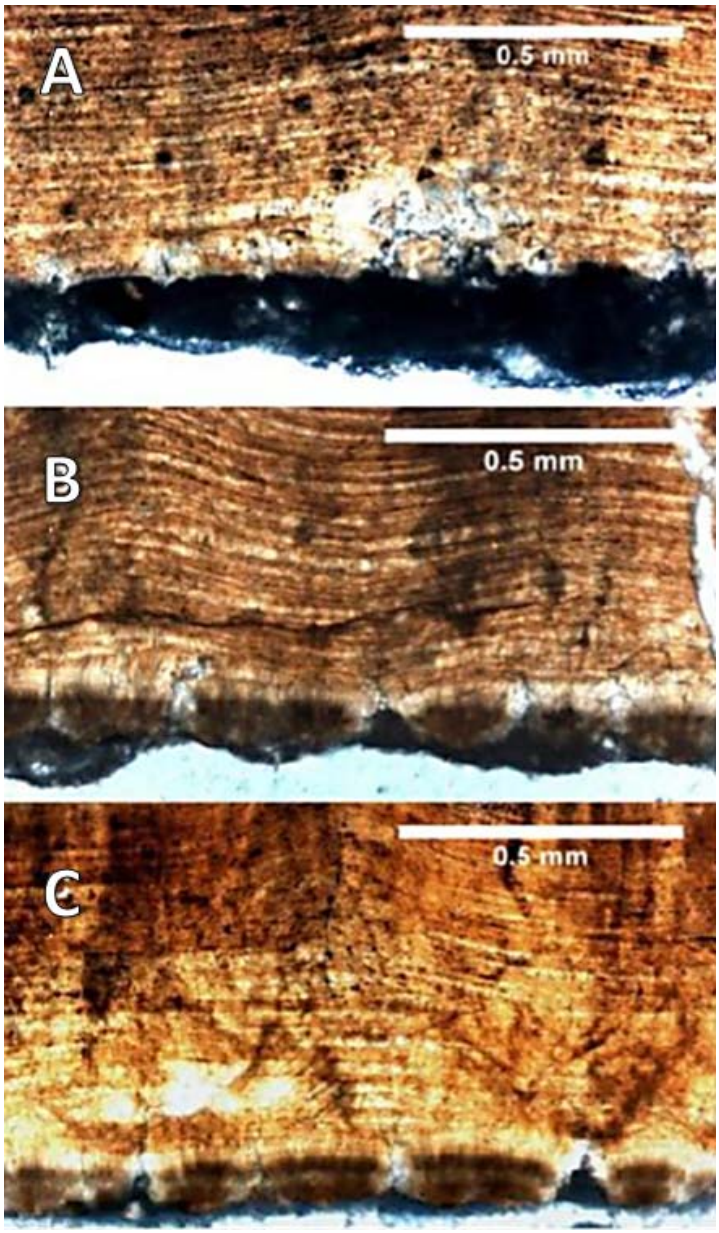


Figure 27. Radial views of MOR 326B. A) Eggshell from wide pole showing reduced mammillary cones. B) Eggshell from equator showing complete mammillary cones. C) Eggshell from tapering pole showing complete mammillary cones.

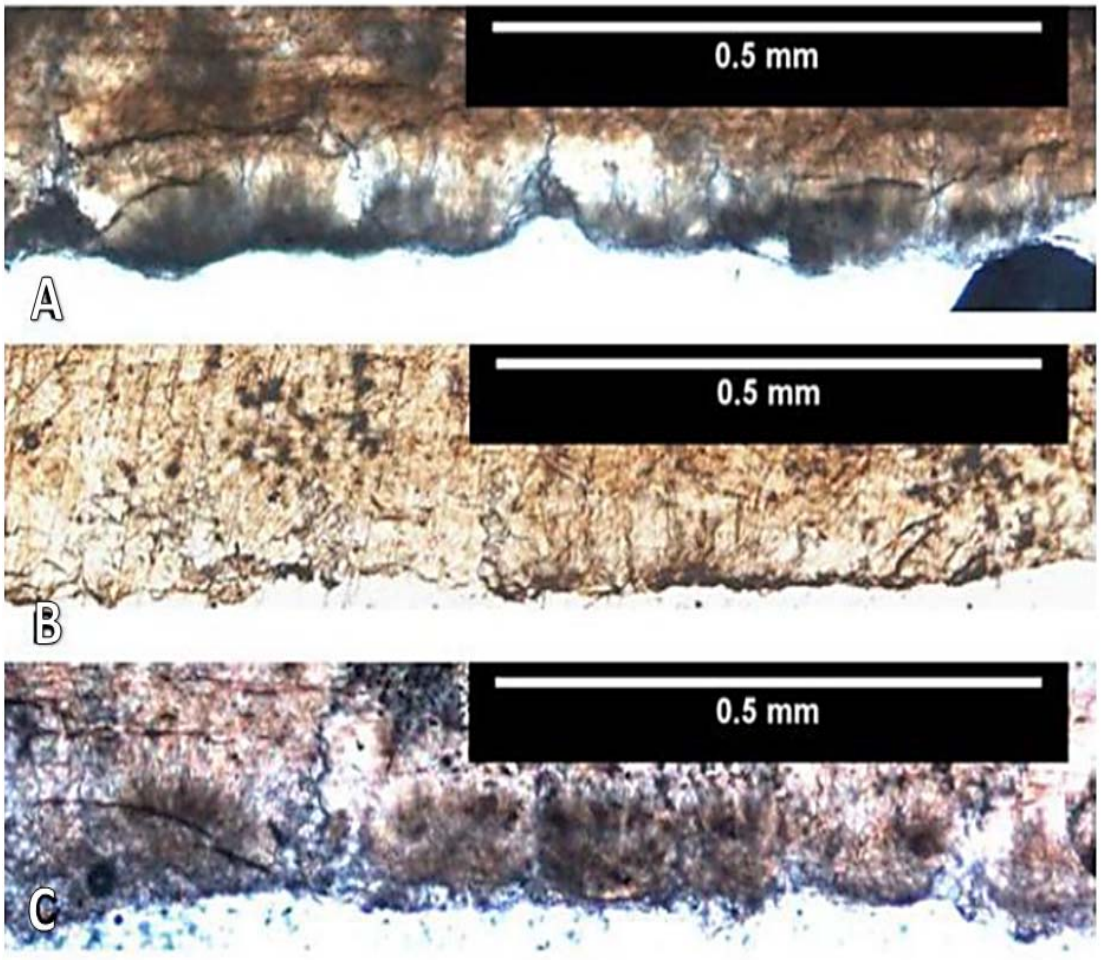


Figure 28.Radial views of MOR 326C. A) Eggshell from wide pole showing relatively complete mammillary cones. B) Eggshell form equator showing significantly reduced mammillary cones. C) Eggshell from tapering pole showing mostly complete mammillary cones.

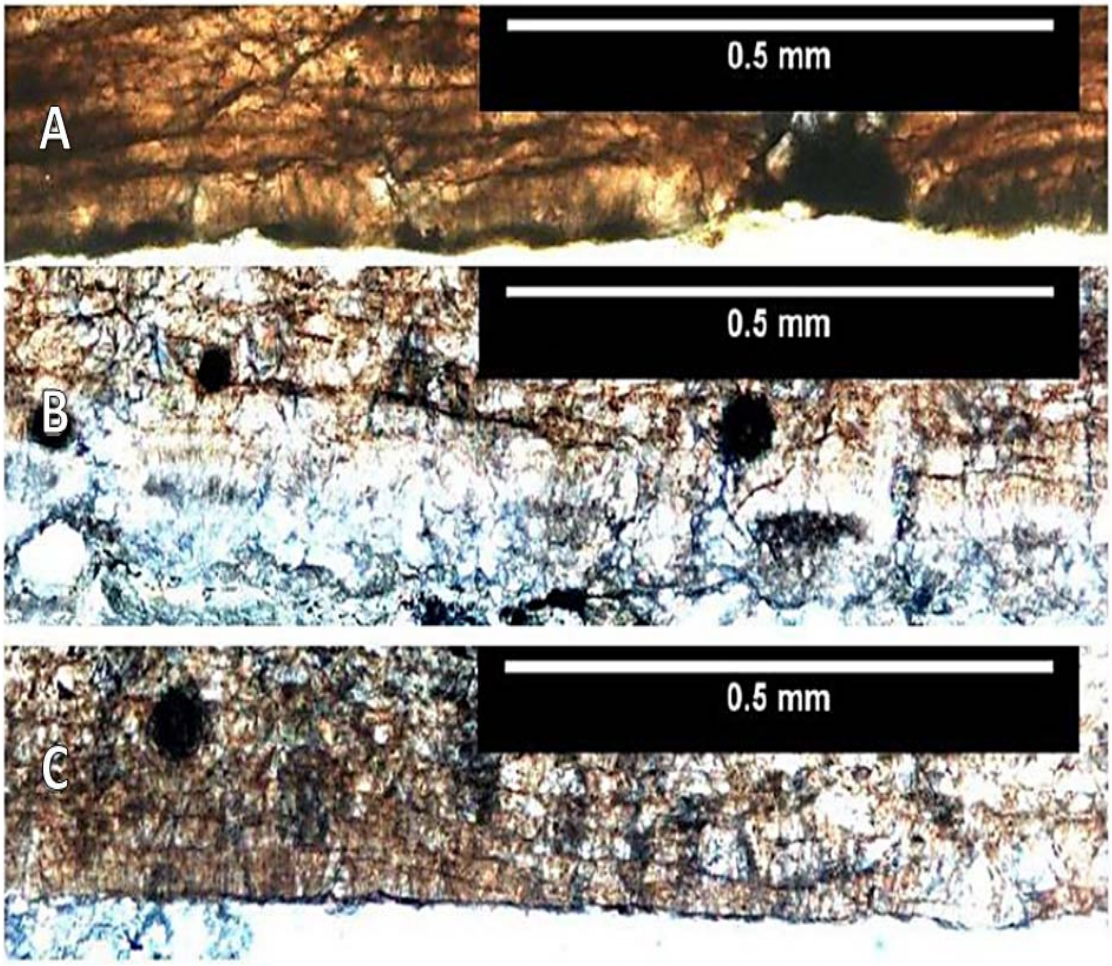


Figure 29. Radial views of MOR 301B. A) Eggshell from wide pole showing reduced mammillary cones. B) Eggshell from equator showing relatively complete mammillary cones. C) Eggshell from tapering pole showing absence of mammillary cones.

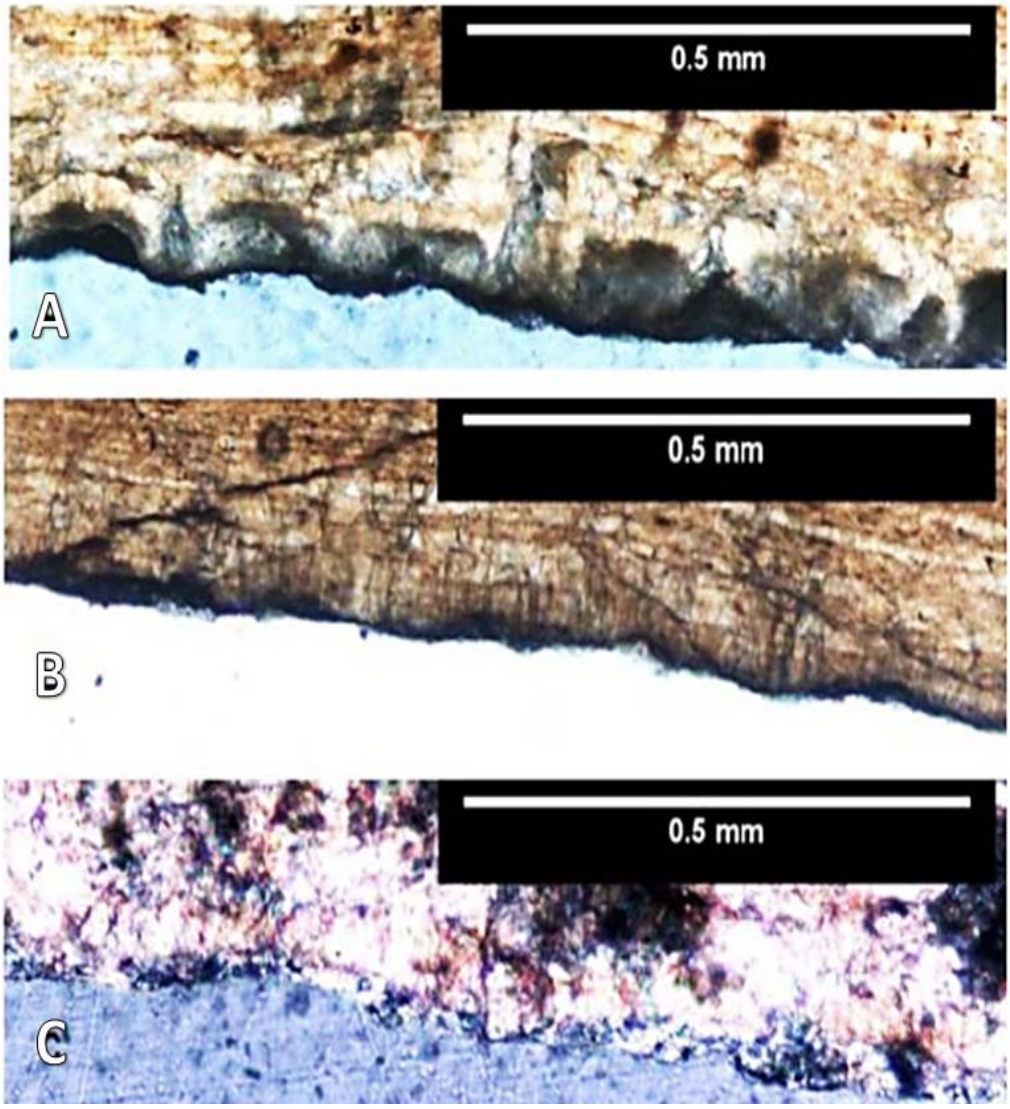


Figure 30. Radial Views of MOR 3062A. A) Eggshell from wide pole showing reduced mammillary cones with some cones essentially complete. B) Eggshell from equator showing that mammillary cones are absent. C) Eggshell from tapering pole showing that mammillary cones are absent.

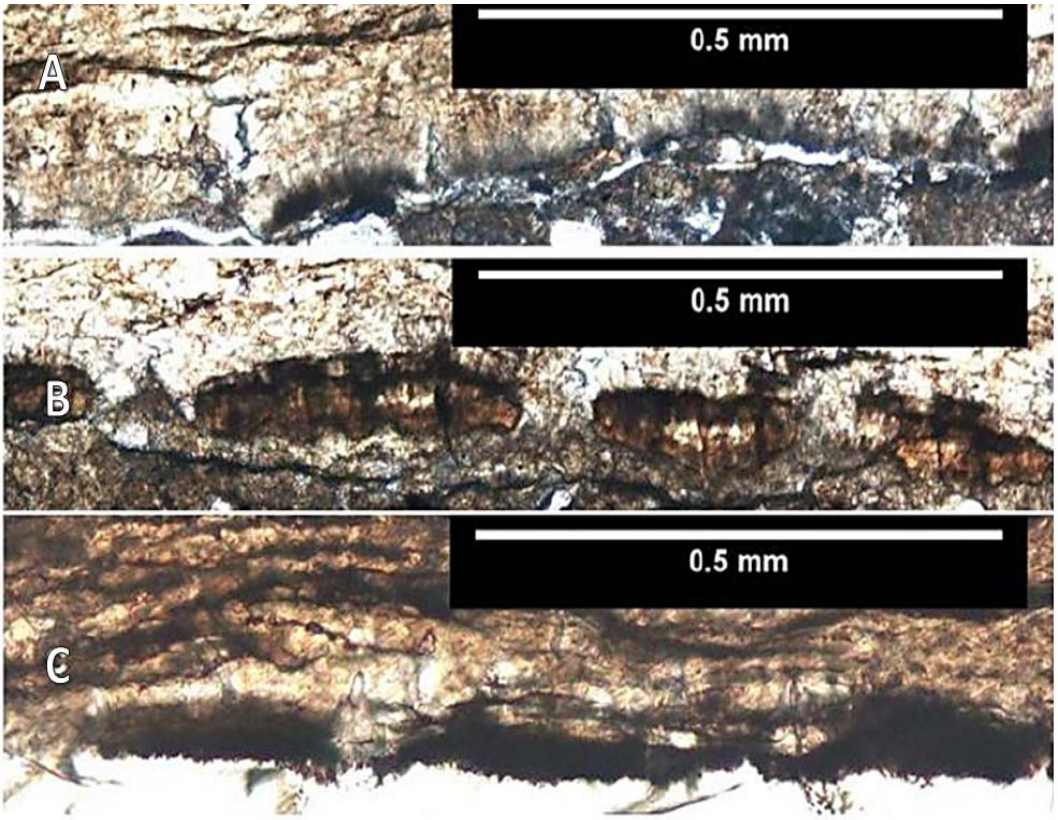


Figure 31. Radial views of YPM-PU. A) Eggshell from wide pole showing reduced mammillary cones with some cones essentially complete. B) Eggshell from equator showing relatively complete mammillary cones. C) Eggshell from tapering pole showing that mammillary cones are significantly reduced.

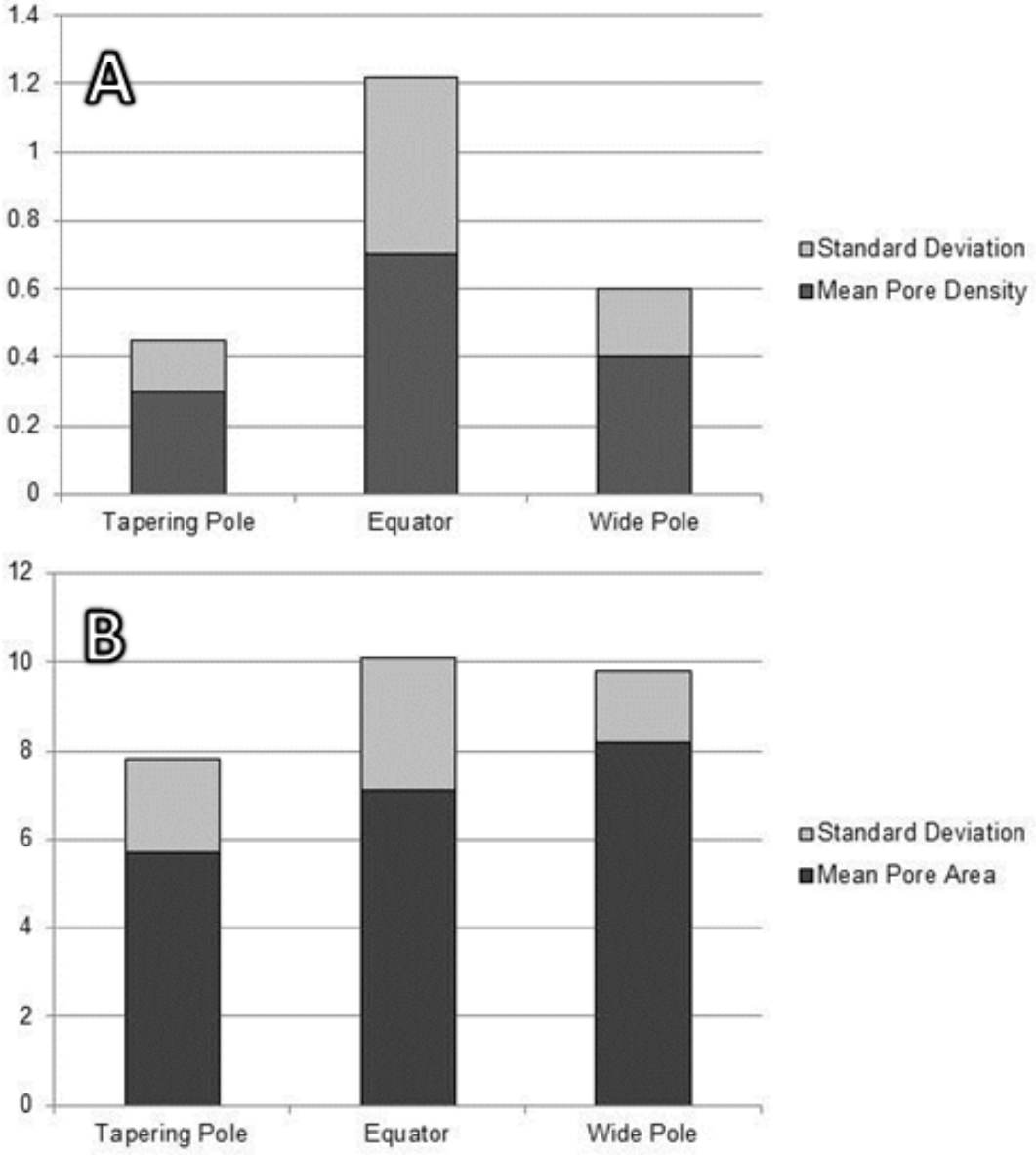


Figure 32. Histograms of pore area and density for all six eggs. A) Histogram of regional mean pore density (pores per mm^2) with standard deviation. B) Histogram of mean individual pore area (mm^2) with standard deviation.

Entire Sample GH2O. Water vapor conductance rates of the six eggs, calculated using all eggshell samples, range from 68-169 mgH_2O/(day Torr), a 2.5x increase from lowest to highest values (Figs. 33-36). Average GH2O for the entire egg is 119 mgH2O/(day Torr)(Table 3). Conductance rates (mgH2O/(day/Torr)) for individual eggs are as follows: MOR 326A (124.531), MOR 326B (122.755), MOR 326C (168.836), MOR 301B (142.893), YPM-PU (88.545), and MOR 3062A (67.597). Regional GH2O values were calculated for 1) the tapering pole, 2) the equator, 3) the wide pole for each egg. Regional GH2O was additionally calculated across the entire set. Values are applied to the whole egg area. MOR 326C exhibits the highest regional water vapor conductance value, 365.91mgH_2O/(day Torr) at the equator. MOR 326C also has the lowest regional GH2O value, 48.76mgH_2O/(day/Torr) at the wide pole. Regional GH2O across the set, listed in Table 5 and illustrated in Figures 33-36, is summarized as follows: mean GH2O (SD) is 75(51) mgH_2O/(day Torr) for the tapering pole, 169(105) mgH_2O/(day Torr) for the equator, and 121(71) mgH_2O/(day Torr) for the wide pole. A histogram of total egg GH2O of the six specimens and standard deviation for each egg is presented in Figure 36.

GH2O Excluding Incomplete Samples. Total egg GH2O, calculated using only samples with complete mammillary layers, varied from 75-170 mgH_2O/(day Torr) across the sample set, a 2.2x increase from lowest to highest values (Fig.). Mean idealized GH2O (SD) is 113 (35) mgH_2O/(day Torr). Conductance rates (mgH_2O/(day/Torr) for individual eggs are as follows; MOR 326A (170.271), MOR 326B (152.590), MOR 326C

(74.727), MOR 301B (138.354), and YPM-PU (83.296). There were no samples of MOR 3062A which contained a complete mammillary layer. Regional mean idealized GH2O (SD) is 100.821(69) mgH_2O/(day Torr) for the tapering pole, 127.68 (36) mgH_2O/(day Torr) for the equator, and 91.83 (0) mgH_2O/(day Torr) for the wide pole. Standard deviation for the wide pole is zero as only one sample from the wide pole contained a complete mammillary layer.

GH2O of Idealized Sample Set. Total egg GH2O, calculated using an idealized shell thickness, varied from 62-159 mgH_2O/(day Torr) across the sample set, a 2.6x increase from lowest to highest values (Figs. 33-35). Mean idealized GH2O (SD) is 113 (35) mgH_2O/(day Torr). Conductance rates (mgH_2O/(day/Torr)) for individual eggs are as follows; MOR 326A (119.825), MOR 326B (120.007), MOR 326C (158.749), MOR 301B (133.504), YPM-PU (82.822), and MOR 3062A (61.925). Regional mean idealized GH2O (SD) is 69.937(49) mgH_2O/(day Torr) for the tapering pole, 152.528 (97) mgH_2O/(day Torr) for the equator, and 115.945 (74) mgH_2O/(day Torr) for the wide pole. Figures 33-36 show histograms of regional GH2O with the idealized mammillary layer for each egg.

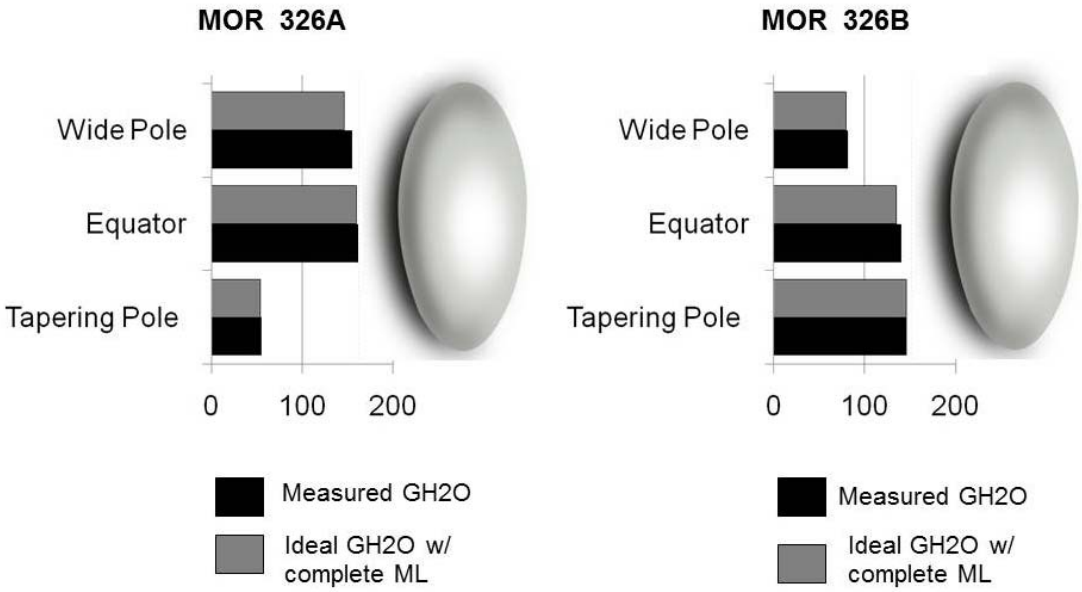


Figure 33. Histogram showing measured regional gas conductance for MOR 326A and MOR 326B. Figure also shows gas conductance for a hypothetical eggshell with complete idealized mammillary layer. X-axis is GH2O in mgH_2O/(day Torr).

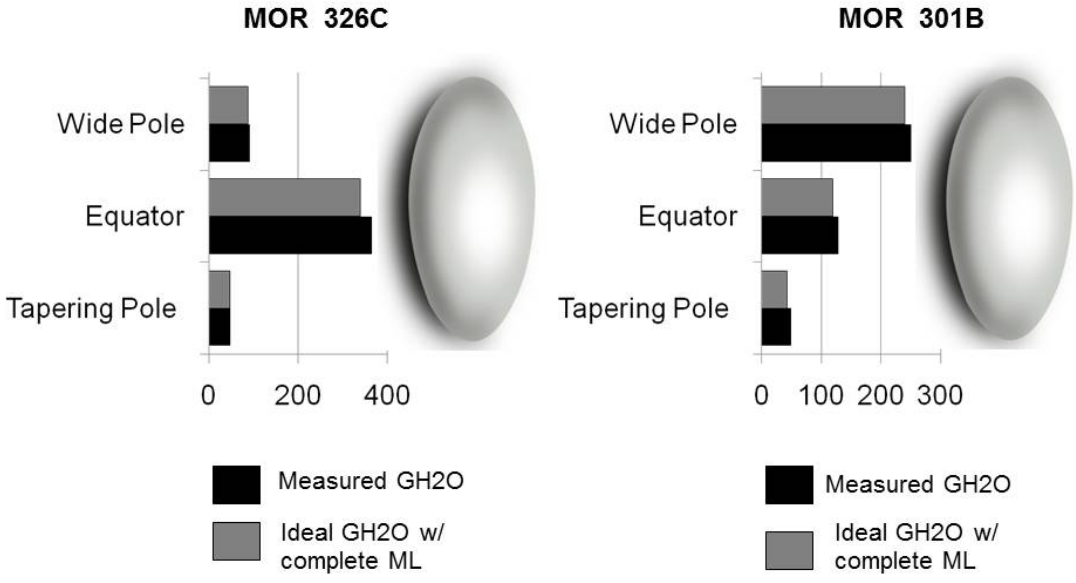


Figure 34. Histogram showing measured regional gas conductance for MOR 326C and MOR 301B. Figure also shows gas conductance for a hypothetical eggshell with idealized mammillary layer. X-axis is GH2O in mgH_2O/(day Torr).

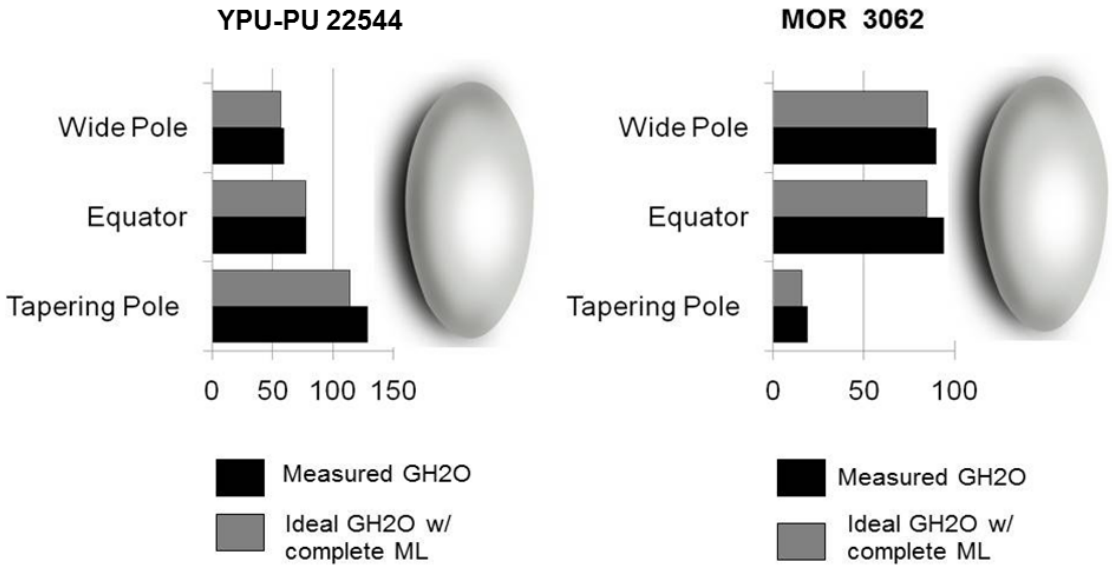


Figure 35. Histogram showing measured regional gas conductance for PU 22544 and MOR 3062. Figure also shows gas conductance for a hypothetical eggshell with idealized mammillary layer. X-axis is GH2O in mgH_2O/(day Torr).

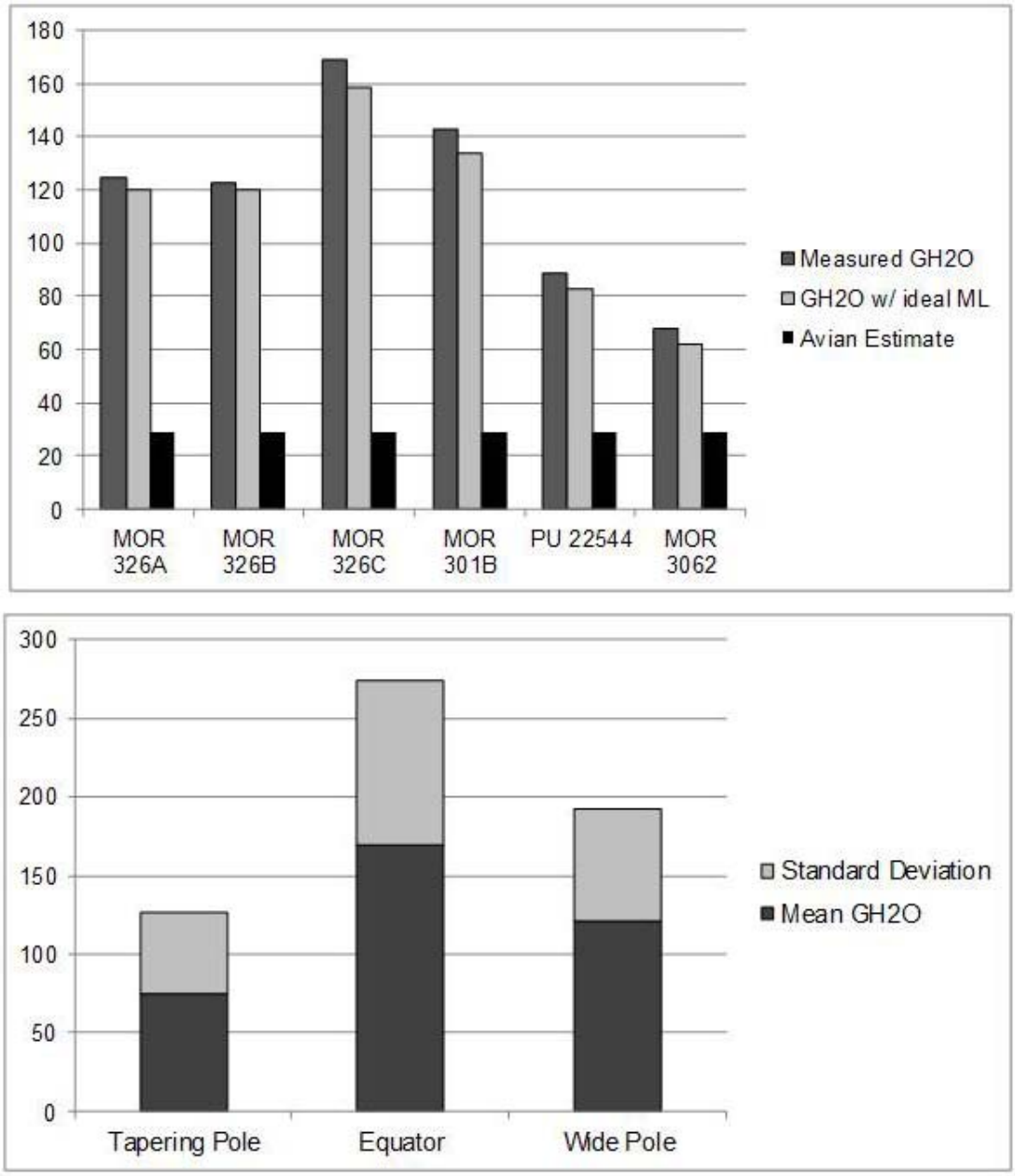


Figure 36. Histograms of GH2O. A) Histogram of water vapor conductance for all six *Continuoolithus canadensis* eggs with standard deviation, with correction for idealized shell thickness estimate, and estimated conductance for a bird egg of equivalent mass B) Histogram of mean regional water vapor conductance with standard deviation.

DISCUSSION

Calculated water vapor conductance values for fossil eggshell have become a common method of determining probable incubation style of non-avian dinosaurs. However, as the study of Jackson et al. (2008) demonstrates, water vapor conductance alone is not strong evidence of one particular incubation strategy. Without the supporting evidence of a nesting trace, eggshell water vapor conductance values provide a rough approximation of incubation environment.

Research on fossil eggs and eggshell indicates that water vapor conductance (Seymour, 1979; Deeming, 2006) and careful geochemical and lithologic descriptions of nesting traces (Varricchio et al., 1999) are valuable tools for determining incubation environment in non-avian dinosaurs. This study provides an estimated water vapor conductance value for *Continuoolithus canadensis*, as well as the geochemistry, mineralogy and taphonomy of the nesting trace containing *C. canadensis* material. Questions addressed in this study, outlined below, are discussed with supporting evidence.

Does Geochemistry and Taphonomy of the MOR 3062 Nesting Trace Provide Evidence of Nesting Site Paleoecology and Microenvironment of the Nest

Analysis of rock samples from the MOR 3062 nest and adjacent mudstone provide evidence for environment and paleoecology of the nesting site. The nest occurs in uniform mudstone, interpreted as deposits resulting from suspension settling of fine

grain sediment on a floodplain some distance from an active stream channel. Evidence indicating relative distance from the stream includes the fining upwards units (Nichols, 1999) of the Flaming Cliffs sequence, capped by a limestone deposit. The mudstone in which the nesting trace occurred showed no evidence of sedimentary structures, which may be due to considerable bioturbation of sediments. Rocks of this substrate are red and oxidized, indicating a well-drained soil. Retallack (1990), however, suggests that this may also indicate soil age, rather than a dry environment. Oxidation of iron was clearly evidenced by staining of rock thin sections. Additional evidence supporting a well-drained soil includes the lack of iron in rhizolith traces (Kraus and Hasiotis, 2006). Rhizoliths within red nodules showed no iron within the actual root traces but significant iron throughout the rest of the nodule. Nodules were enriched in iron relative to the surrounding mudstone in which the nodules occurred. This condition of the rhizolith and surrounding mudstone are typical of surface-water gley processes that cause iron to migrate from the root outward to the surrounding sediments (Kraus and Hasiotis, 2006). Such traces are common in moderately well-drained red paleosols (Kraus and Hasiotis, 2006). Presence, and size, of abundant rhizoliths within the red mudstone support an interpretation of paleoenvironment with abundant small plants. Preservation of other organic traces in these red sediments would be unlikely due to higher microbial action in an oxidized environment (Retallack 1990), and indeed, organic carbon comprised only 0.01% of the red mudstone sampled. Within the nest, various fragile plant structures were preserved. Gypsum and anhydrite were also present in the red mudstone and may represent primary chemical precipitates or secondary diagenetic accumulations due to

weathering. Possible clays within the mudstones of the nesting site include sepiolite, and muscovite or illite.

The green mudstone nesting trace fill that forms a bowl-shaped depression, clearly contrasts with the red mudstone that it truncates. This same relationship was noted in the Maiasaura nesting trace reported by Horner and Makela (1979). Carpenter (1999) suggested that, in the case of the Maiasaura nest, iron in the soil was reduced yielding a green coloration. Conversely, the truncated red sediments would contain iron in an oxidized state. The lack of oxidation in the trace fill may have been due to high moisture content, the decay of organic matter, or both (Carpenter, 1999). Iron reduction, resulting in this green color, would support a high humidity/low oxygen environment (Carpenter, 1999). The extent of the green color in the *Continuoolithus canadensis* nest probably defines the area which experienced reducing conditions. Reducing conditions rarely occur in well-drained, oxidized sediments (Retallack 1990). Because the entire MOR 3062 nesting trace fill displays this green mudstone, the conditions within the nest were likely reducing; this interpretation is supported by the presence of coalified plant material within the trace fill, but not in adjacent strata. This organic material was unlikely to preserve in well-drained, oxidized sediments (Retallack, 1990) such as the red mudstone adjacent to the trace. Further support for this interpretation includes stained slides of the trace fill and red mudstone which showed reduced and oxidized iron, respectively. Analyses (TOC and EDS) confirm that organic carbon was much higher in the trace than in the adjacent red mudstone. The only exceptions are the rhizolith-bearing nodules, within the red mudstone, which exhibit high carbon content, likely organic

residue of roots.

Other chemical differences that distinguish the nesting trace fill from the red mudstone include 1) the presence of gypsum and anhydrite in red mudstone, but not within the trace; and 2) greater abundance of calcite and albite in the red mudstone than present in the nesting trace.

What Was the Incubation Method Used By the Theropod Which Constructed the MOR 3062 Nesting Trace

Evidence supports incubation of *Continuoolithus canadensis* eggs as buried in substrate. Geochemistry shows that the nesting trace contained highly reduced iron. Sub-aerial exposure of sediments would have resulted in oxidation and red coloration as was the case for the unit truncated by the nest fill and the unit overlying the nest. For the creation of a reducing microenvironment some barrier likely separated the clutch from the ambient atmosphere. This might have been sediment encasing and covering the clutch, plant debris covering the clutch, or a combination of the two. Presence of a horizontal organic band within the nest, nearly adjacent to the clutch, supports one of the latter. Sabath (1991) suggests that nodes and high relief sculpturing on fossil eggs may facilitate gas exchange where pores would otherwise be occluded by vegetation. Grellet-Tinner et al., (2006) suggest that where fine-grained sediment (i.e. those used to cover and incubate eggs) is smaller than the intermodal distance necessary for pores to be functional, vegetation would be needed as a buffer to allow gas exchange. Therefore, a scenario whereby the parent buries eggs in sediment along with vegetation is not

unreasonable. A purported sauropod clutch (Vila et al., 2009), interpreted as incubated in a substrate, also contains eggs of a nodular texture that was associated with carbonized, small, fragments of indeterminate plants. However, eggs of extant reptiles, buried in substrate do not show ornamentation (Jackson et al., 2008). Additional support for a buried incubation environment includes the scarcity of eggshell fragments within the nest, other than the compressed and fragmentary eggs of the clutch. Mueller-Towe et al. (2002) consider the lack of scattered small eggshell fragments evidence for underground incubation because eggshell material in an above ground nest would presumably be fed upon, broken, and trampled, leaving no large pieces intact. Alternately, in a buried nest, eggshell fragments would not be trampled and broken and would be largely restricted to the hatching location.

The most reasonable explanation for the taphonomic and geochemical data related to MOR 3062 is that the parent excavated a bowl-shaped depression in a well-drained floodplain soil. She then deposited her eggs and back-filled the depression with plant debris and possibly loose sediment. Over time, the decay of the plant matter, and possibly the decay of the eggs, created reducing conditions surrounding the clutch. This resulted in the green mudstone trace fill. Figure 37 illustrates how the clutch was preserved in the fossil record.

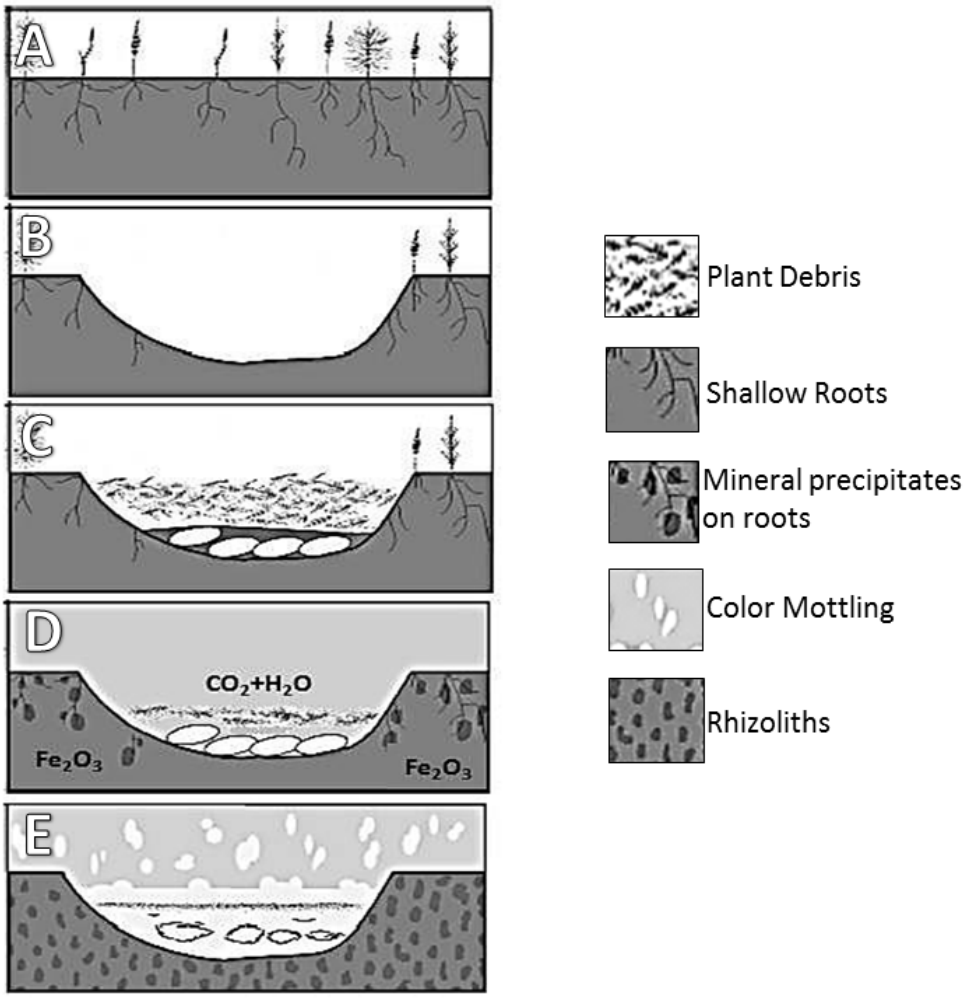


Figure 37. Illustration showing MOR 3062 nest construction and preservation process. A) Well-drained floodplain paleosol with vegetative cover. B) Bowl-shaped depression is excavated. C) Eggs are laid and covered with sediment and plant debris. D) Mud buries the trace and substrate. Within the trace, rotting organic material contributes to the reducing environment (CO_2+H_2O). Adjacent to the trace, the paleosol shows oxidation of sediments (Fe_2O_3). E) The preserved trace. Lens measures approximately 43 cm in diameter at widest point.

Do the Descriptions of *Continuoolithus canadensis* Clutch Arrangement, Egg Gross Morphology, and Eggshell Microstructure in This Study Agree With Earlier Research

I interpret the MOR 3062 nesting trace as containing the remains of four unhatched eggs. This interpretation is based on the size of eggshell pieces and egg portions, the orientation of the fragments within the sediment, and the three-dimensional ovoid geometry of discreet clusters of fragments and portions. All eggs were lithostatically compressed. All four eggs lay with their long axis parallel to the lower surface of the nesting trace. The long axes of three of the eggs were parallel to one another and the fourth was perpendicular. Eggs were spaced 2-3 cm apart. Hirsch and Quinn (1990) report *Continuoolithus canadensis* clutches with 3 and 6 eggs. The clutch of three is MOR 326 (Fig. 38). In the MOR 326 clutch, two eggs are closely spaced with their long axes parallel, whereas the long axis of the third egg is perpendicular. Horner (1987, 1997) describes these eggs as arranged in paired linear rows; however, no specimen numbers or photographs are provided thus prohibiting comparison to eggs in the current study.

Egg size and shape cannot be compared to Zelenitsky et al. (1996) because of the fragmentary condition of Alberta *Continuoolithus canadensis* material. Eggs in the current study are ovoid in shape, with one pole narrower than the other. However, previous studies describe eggs of this oospecies as oval, elongate, having a pointed end (Hirsch and Quinn, 1990); Horner (1997) described these eggs as ellipsoid.

On the basis of microstructural characteristics, eggs from the WCA conform to the oospecies definition of *Continuoolithus canadensis* (Zelenitsky et al., 1996). However, prismatic columns have not been noted in previous studies of this oospecies. Hirsch and Quinn (1990) describe shell thickness of *C. canadensis* as 1.2-1.28 mm (including node height), whereas Zelenitsky et al. (1996) report 0.94-1.24 mm, including ornamentation. Based on a limited sample size, Jackson and Varricchio (2010) report that thickness of possible *C. canadensis* varies from 0.86 mm between nodes to 1.20 mm over nodes. Eggshells in the present study are 0.65-1.22 mm (including node height) and 0.64-1.08 mm between nodes. Pore diameter also varies among studies. Hirsch and Quinn (1990) reported pores between 0.15-0.16 mm in diameter, whereas this value is not reported in Zelenitsky et al. (1996). However, SEM images in Zelenitsky et al. (1996) show that several pores are 0.09 mm in diameter. Jackson and Varricchio (2010) report pores from 0.1 mm to 0.2 mm in diameter. Pores in the present study range from .051 mm to .167 mm in diameter. One pore widened to 0.201 mm mid-way through the shell, although this likely resulted from diagenetic dissolution. Mammillary to continuous layer ratios reported in previous studies ranged from 1:4-5 (Zelenitsky et al., 1996) to 1:6 (Jackson and Varricchio, 2010) to 1:10-12 (Hirsch and Quinn, 1990). The mammillary to continuous layer ratios in this study are 1:6-1:13 including node height and 1:5-1:11 between nodes.

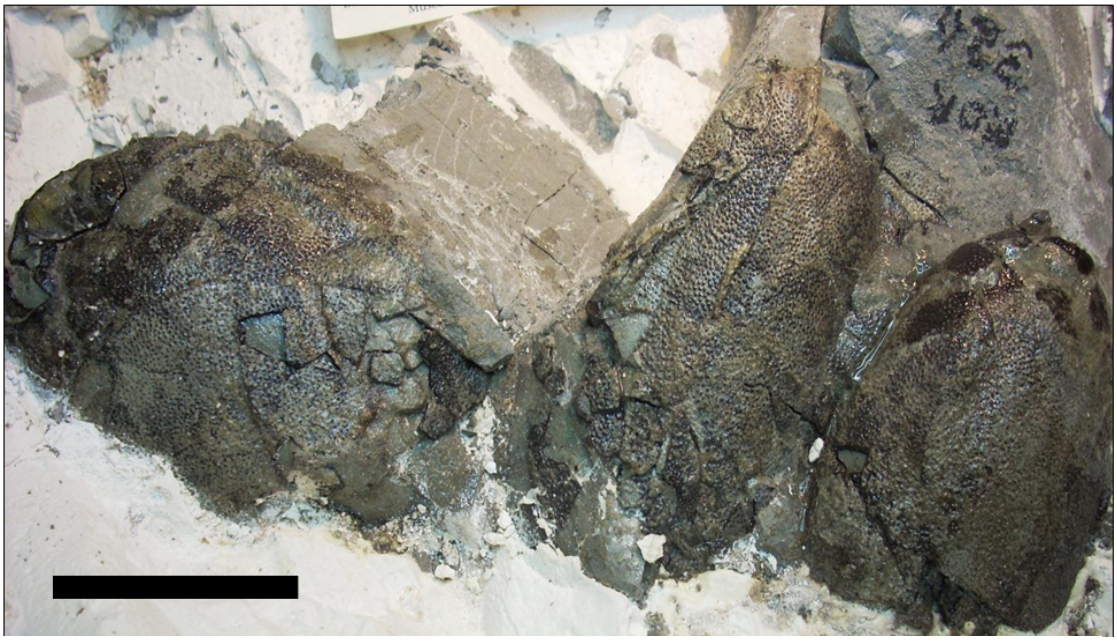


Figure 38. MOR 326 clutch showing three eggs and their arrangement. Scale measures 5 cm.

What is the Water Vapor Conductance Rate for *Continuoolithus canadensis* Eggshell Would This Water Vapor Conductance Rate be Higher or Lower for a Bird Egg of Equal Mass

Actual measurements obtained from the eggshells show a 2.5x increase between the lowest and highest water vapor conductance values for all eggs, with a mean GH2O for all eggs of 119 mgH_2O/(day Torr). The predicted water vapor conductance value for a bird egg of the same mass is 29 mgH_2O/(day Torr), as calculated using the regression formula from Jackson et al. (2008). This equates to a 4.1 times greater mean GH2O in *Continuoolithus canadensis* eggs than a bird egg of the same mass.

Did Modification (Diagenetic and/or Biologic) of *Continuoolithus canadensis* Eggshell Significantly Affect the Calculation of Water Vapor Conductance

Several factors influence calculation of water vapor conductance: shell thickness, pore density, pore area, and surface area of the egg. For example, thickness may be affected by mammillary layer reduction. Of the 18 locations sampled (3 samples for each of 6 eggs), only 7 possessed complete mammillary layers. Mammillary layer reduction may result in part from utilization of calcium by the embryo during incubation and/or later diagenetic dissolution. It is not a goal of the present study to distinguish between these causes. To determine what effect reduction of the mammillary layer has on overall water vapor conductance in this type of egg, an idealized mammillary layer thickness (0.15 mm) was used to calculate GH2O. Measurements obtained from the eggshells show a 2.5x increase between the lowest and highest water vapor conductance values for all eggs, with a mean GH2O for all eggs of 119 mgH_2O/(day Torr). The same measurements, using an idealized mammillary layer, show a 2.6x increase, with a mean GH2O for all eggs of 113 mgH_2O/(day Torr). If samples with absent or reduced mammillary layers are excluded, a 2.2x increase is observed between the lowest and highest water vapor conductance values, with a mean GH2O for all eggs if 113 mgH_2O/(day Torr). This indicates that calculation of GH2O is not significantly affected by reduction in shell thickness because the mammillary layer represents only a small proportion of the intact shell thickness.

Does the Microstructure and Water Vapor Conductance Value for *Continuoolithus canadensis* Support the Interpretation of Incubation Strategy Provided by the MOR 3062 Nesting Trace

The substantially higher water vapor conductance of *Continuoolithus canadensis* compared to a modern bird egg of equivalent mass indicates a different style of incubation. High water vapor conductance values are characteristic of reptile eggs that are buried in sediments or vegetation mounds (Seymour and Ackerman, 1980; Deeming 2002, 2004). For example, alligator (*Alligator mississippensis*) and turtle (*Trionyx spiniferus* and *Emydura macquarii*) eggs exhibit GH2O of 2,902 mgH_2O/(day Torr) and 810-1268 mgH_2O/(day Torr), respectively, (Packard et al., 1979; Harrison et al., 1978; Thompson, 1985). These values are 4.2 and 5.46-8.3 times the values expected for an avian egg of comparable mass, respectively. Some avian eggs exhibit higher GH2O values than predicted for an avian egg of comparable mass incubated in the typical sub-aerial manner; for example, megapode eggs that are buried in vegetation (Booth and Seymour, 1987) and those of burrowing birds (Birchard and Kilgore, 1980) exhibit rates of 2.5 and 1.2 times greater than a bird egg of equivalent mass, respectively (Birchard and Kilgore, 1980; Seymour et al., 1986; Booth and Seymour, 1987). Because *C. canadensis* has substantially higher water vapor conductance values than that predicted for a bird egg of the same mass, it is likely that *C. canadensis* incubated eggs in the substrate or in vegetation rather than sub-aerially exposed.

Additional evidence for a buried incubation environment is the presence of nodes covering *Continuoolithus canadensis* eggs. Nodes sometimes represent 20% of the total

eggshell thickness. One or more pores surround the base of a given node. This association between nodes and pores had been described from purported sauropod eggs believed to have been incubated in substrate (Vila et al., 2009). Sabath (1991) speculated that eggshell surface sculpturing could act as a buffer between vegetation in the nest and the pore's opening. This could explain the close association of the nodes to pore openings; the nodes may prevent debris from blocking gas exchange. This is also consistent with an incubation interpretation where the eggs are buried in vegetation or fine sediment). Unfortunately, no eggs of extant birds or reptiles display such nodes, therefore a possible correlate is not available.

What Assumptions and Errors Potentially Influence Findings of this Study

Mean values were calculated for regional and whole eggshell thickness, pore area, pore density and GH2O, along with standard deviations. From these, confidence intervals were determined for GH2O across all six eggs and for the three individual regions. The confidence interval for all six eggs' mean GH2O at a 95% level is +/- 66.01 mgH_2O/(day Torr). For the individual regions the confidence intervals at a 95% level were; +/- 40.48 mgH_2O/(day Torr) (tapering), +/- 83.79 mgH_2O/(day Torr) (equator), and +/- 56.61 mgH_2O/(day Torr) (wide). Both *t*-values and *P*-values were calculated with 10 degrees of freedom for the null hypothesis, which is that there is no regional change in GH2O and that the mean GH2O for any region is equal to mean GH2O for the whole egg. The *P*-value for the tapering region is 0.92, for the equator 0.25 and for the wide

region 0.48. These *P*-values do not reject the possibility that the null hypothesis is correct. Examination of a histogram of regional GH2O and its standard deviation verifies that there is great variability and that patterns of regional GH2O could be random.

Confidence intervals, *t*-values, and *P*-values were also calculated for pore density and shell thickness, where the null hypothesis is that regional measurements will not differ significantly from whole egg mean. Confidence intervals for regional shell thickness with a 90% confidence level are +/- 0.08 mm for the tapering region, +/- 0.07 mm for the equator, and +/- 0.07 mm for the wide region. *P*-values for each region are 0.71 for the tapering region, 0.60 for the equator, and 0.83 for the wide region. As with GH2O, these *P*-values do not reject the possibility that the null hypothesis is correct. These results indicate that although regional patterns of shell thickness, pore area, GH2O and pore density are observed, these patterns are not necessarily statistically significant and may be artifacts due to the variable nature of pore density, pore area, shell thickness, and insufficient sample sizes. Further, because these eggs came from multiple clutches, the standard deviation may reflect inter-clutch differences.

Several assumptions were made which define the limitations of this study. One such assumption is that measurements of the three regions sampled can be weighted equally and averaged. However, each region does not necessarily contain the same surface area, and measured features may change notably within the arbitrarily defined region. Weighting regional GH2O by percentage of surface area included in that region would produce a more accurate total mean egg GH2O. For more accurate measurement, multiple samples should be analyzed from each region, as microstructure may change

across the region. Further sampling would also help to mitigate the effect anomalous samples have on calculation of GH2O. Another assumption is that regional GH2O can be calculated using measurements for pore area, pore density and shell thickness from the three defined egg locations (tapering pole, equator, wide pole) but applied to total egg surface area. This introduces error in that representing a whole egg's GH2O, based on one region's measurements, ignores variation present within the rest of the egg and either over or under estimates GH2O. Such calculations are only approximations for comparison between regional measurements and whole egg measurements. Despite the lack of statistical significance, the trends seen in regional differences in shell thickness, pore distribution, and conductance indicate that further investigation may verify these differences and shed more light on incubation practices.

Some modern avian eggs show regional decline in both conductance and pore density from the wide pole to the pointed pole (Rokitka and Rahn, 1987), a different pattern than observed in *Continuoolithus canadensis*. However, mute swan eggs show an increase in pore density and GH20 at the equator (Booth, 1989), similar to *C. canadensis*. American alligator (*Alligator mississippiensis*) eggs show no change in shell permeability throughout incubation (Kern and Ferguson, 1997). However, an internal shell membrane quadruples in permeability throughout incubation, with permeability notably higher at the equator (Kern and Ferguson, 1997). No such change in permeability is seen for the estuarine crocodile (*Crocodylus porosus*) (Grigg and Beard, 1985). The shell membrane in alligators and crocodiles is thicker than that of modern avians (Grigg and Beard, 1985).

As this membrane is not preserved in *C. canadensis*, it is impossible to determine what influence it might have exerted over water vapor conductance.

CONCLUSIONS

The nesting trace containing *Continuoolithus canadensis* eggs provides rare paleobiologic insight into the parental behavior of an extinct organism. Geochemistry indicates that iron within the trace is in a reduced state whereas iron in the adjacent mudstone is in an oxidized state. Vegetative debris occurs within the trace but not in the adjacent mudstone, whereas iron-rich mudstone nodules containing rhizoliths are found in the adjacent mudstone but not in the trace. The distinct geochemistry of the trace fill, and presence of partial eggs and eggshells, indicates this structure represents a nest excavated by the adult for the purpose of egg-laying. Presence of a band of condensed vegetative material within the trace indicates organic matter was incorporated into the structure either through active inclusion by the parent or through depositional processes. Eggshell material within this trace likely represents clutch of *in situ* compressed eggs.

The eggs in this study conform to the oospecies *Continuoolithus canadensis* as described by Zelenitsky et al. (1996). Measurements of eggshell thickness, pore diameter, and continuous layer to mammillary ratio are consistent with ranges previously reported by Hirsch and Quinn (1990), Zelenitsky et al. (1996), and Jackson and Varricchio (2010). Comparison of thickness and GH2O among eggshell samples with reduced mammillary layers and complete samples showed little effect on regional or overall water vapor conductance because reduction did not change pore morphology or substantially shorten pore length. Mean regional measurements showed no significant patterns in GH2O between the tapering pole, the equator, and the wide pole of *C.*

canadensis eggs. Additionally, regional GH2O varied notably from egg to egg and mean regional GH2O displayed very high standard deviation across the entire sample set. Association of pores with nodes was clearly observed and, in conjunction with the nesting trace's organic content, provides support for Sabath's (1991) hypothesis for node function.

The relationship between water vapor conductance and incubation strategy in extant species provides a basis for assessing *Continuoolithus canadensis* egg incubation. The average water vapor conductance of 119 mgH_2O/(day Torr) is 4.1 times greater than predicted for a bird egg of equivalent mass. High water vapor conductance values for *Continuoolithus canadensis* support the interpretation that eggs were incubated in a humid microenvironment. Comparable examples today include eggs of reptiles buried in sediment or vegetation mounds. Evidence presented in this study indicates that the producer of *C. canadensis* constructed a bowl-shaped structure within a soil, deposited eggs within that structure, and likely covered the structure with sediment and plant material.

This study provides a unified approach for understanding *Continuoolithus canadensis* egg physiology and reproductive behaviors of the adult, combining sedimentology of the nesting structure and microstructural study of the egg, including water vapor conductance rate.

REFERENCES CITED

Ackerman, R 1980. Physiological and ecological aspects of gas exchange by sea turtle eggs. American Zoologist 20:575–583.

Ar, A., C.Paganelli, R. Reeves, D. Greene, and H. Rahn. 1974. The avian egg: water vapor conductance, shell thickness, and functional pore area. Condor 76:153–158.

Ar, A., and H. Rahn.1985. Pores in avian eggshells: Gas conductance, gas exchange and embryonic growth rate. Respiration Physiology 61:1-20.

Birchard, G. and D. Kilgore. 1980. Conductance of water vapor in eggs of burrowing and non-burrowing birds: implications for embryonic gas exchange. Physiological Zoology 53:284-292.

Board, R. and V. Scott. 1980. Porosity of the avian eggshell. American Zoologist, 20:339-349.

Booth, D. 1989. Regional changes in shell thickness, shell conductance, and pore structure during incubation in eggs of the Mute Swan. Physiological Zoology 62:607-620.

Booth, D. and R. Seymour. 1987. Effect of eggshell thinning on water vapor conductance of Mallee fowl eggs. The Condor 89:453-459.

Carpenter, K. 1999. Eggs, Nests, and Baby Dinosaurs: A Look at Dinosaur Reproduction, Indiana University Press, Bloomington, Indiana.

Chiappe, L., L. Dingus, F. Jackson, G. Grellet-Tinner, R. Aspinall, J. Clarke, R. Coria, A. Garrido, D. Loope. 2000. Sauropod eggs and embryos from the Late Cretaceous of Patagonia. I Symposium of Dinosaur Eggs and Embryos, Isona, Spain, 23-29 pp.

Chiappe, L. R. Coria, F. Jackson, L. Dingus. 2003. The Late Cretaceous nesting site of Auca Mahuevo (Patagonia, Argentina): eggs, nests, and embryos of titanosaurian sauropods. Palaeovertebrata, Montpellier 32:97-108.

Chiappe, L., J. Schmitt, F. Jackson, A. Garrido, L. Dingus, G. Grellet-Tinner. 2004. Nest structure for sauropods: Sedimentary criteria for recognition of dinosaur nesting traces. Palaios 19:89-95.

Cousin, R., G. Breton, R. Fournier, and J. Watte. 1994. Dinosaur egglaying and nesting in France. In Carpenter, K., Hirsch, K., and Horner, J. (eds): Dinosaur Eggs and Babies, 56–74. Cambridge University Press, Cambridge.

Deeming, D and M. Thompson. 1991. Gas exchange across reptilian eggshells. In Deeming, C. and Ferguson, M. (eds): Egg incubation: its effects on embryonic development in birds and reptiles, 277-283. Cambridge University Press, Cambridge.

Deeming, R. 2002. Avian incubation: behavior, environment, and evolution. Oxford University Press, Oxford, 421 pp.

Deeming, R. 2004. Reptilian incubation: environment, evolution and behavior, Nottingham University Press, Nottingham, 349 pp.

Deeming, R. 2006. Ultrastructural and functional morphology of eggshells supports the idea that dinosaur eggs were incubated buried in a substrate. Palaeontology 49:171–185.

Donaire, M., and N. López-Martínez. 2010. Porosity of Late Paleocene *Ornitholithus* eggshells. (Tremp Formation, south-central Pyrenees, Spain). Palaeoclimatic implications. Palaeogeography, Palaeoclimatology, Palaeoecology 279:147-159.

Fink, R., and J. Schmitt. 1999. Fluvial channel systems of the Upper Cretaceous (Campanian) Two Medicine Formation, Willow Creek Anticline, Choteau, MT, USA. American Association of Petroleum Geologists Search and Discovery Article #90919. American Association of Petroleum Geologists Rocky Mountain Section Meeting, Bozeman, Montana.

Flugel, E. 2004. Microfacies of carbonate rocks: analysis, interpretation and application. Springer, New York, 163 pp.

Gill, J. and W. Cobban. 1973. Stratigraphy and geologic history of the Montana Group and equivalent rocks, Montana, Wyoming and North and South Dakota: United States Geological Survey, Professional Paper, no. 776.

Grellet-Tinner, G., L. Chiappe, M. Norell, D. Bottjer. 2006. Dinosaur eggs and nesting behaviors: A paleobiological investigation. Palaeogeography, Palaeoclimatology, Palaeoecology 232:294-321.

Grigg, G. and L. Beard. 1985. Water loss and gain by eggs of *Crocodylus porosus*, related to incubation age and fertility. In Grigg, B., Shine, R., and Ehmann, H. (eds): Biology of Australasian frogs and reptiles, 353-359. Surry Beatty, Sydney.

Gwinn, V. and T. Mutch. 1965. Intertongued Upper Cretaceous volcanic and nonvolcanic rocks, central-western Montana. Geological Society of America Bulletin, 76:1125-1144.

Harrison, K., T. Bently, P. Lutz, and D. Marszalek. 1978. Water and gas diffusion in the American crocodile egg. American Zoologist 18:637.

Hirsch, K. and B. Quinn. 1990. Eggs and eggshell fragments from the Upper Cretaceous Two Medicine Formation of Montana. Journal of Vertebrate Paleontology, 10:491-511.

Horner, J. 1987. Ecological and behavioral implications derived from a dinosaur nesting site. In Czerkas, S., Olson, E. (eds): Dinosaurs Past and Present in Dinosaurs Past and Present, Volume II, 51-63. University of Washington Press, Seattle.

Horner, J. 1997. Rare preservation of an incompletely ossified fossil embryo. Journal of Vertebrate Paleontology 17:431-434.

Horner, J. 2000. Dinosaur reproduction and parenting. Annual. Review of Earth and Planet. Sciences 28:19–45.

Horner, J. and R. Makela. 1979. Nest of juveniles provides evidence of family structure among dinosaurs. Nature 282:296–298.

Hoyt, D. 1987. The effect of shape on the surface-volume relationships of bird. Condor 78:343-349.

Jackson, F. and D. Varricchio. 2010. Fossil eggs and eggshell from the lowermost Two Medicine Formation of western Montana, Sevenmile Hill locality. Journal of Vertebrate Paleontology, 30:4:1142-1156.

Jackson, F., D. Varricchio, R. Jackson. B. Vila, L. Chiappe. 2008.Comparison of water vapor conductance in a titanosaur egg from the Upper Cretaceous of Argentina and a *Megaloolithus siruguei* egg from Spain. Paleontological Society 34:229-246.

Kern, M., and M. Ferguson. 1997. Gas permeability of American alligator eggs and its anatomical basis. Physiological Zoology 70:530–546.

Kraus, M. and S. Hasiotis. 2006. Significance of different modes of rhizolith preservation to interpreting paleoenvironmental and paleohydrologic settings: examples from Paleogene paleosols, Bighorn Basin, Wyoming, U.S.A. Journal of Sedimentary Research 76:3:633-646.

Lageson, D., J. Schmitt, B. Horton, T. Kalakay, and B. Burton. 2001. Influence of Late Cretaceous magmatism on the Sevier orogenic wedge, western Montana. Geology, 29:723-726.

Lorenz, J. 1981. Sedimentary and tectonic history of the Two Medicine Formation, Late Cretaceous (Campanian), northwestern Montana. Princeton, N.J., Princeton University, Ph.D. dissertation, 225 pp.

Lorenz, J. and W. Gavin. 1984.The geology of the Two Medicine Formation and the sedimentology of a dinosaur nesting ground. In McBane, J. and Garrison, P. (eds): Northwestern Montana and Adjacent Canada: Montana Geological Society 1984 Field Conference and Symposium, 175-186 pp.

Mikhailov, K., E. Bray, K. Hirsch. 1996. Parataxonomy of fossil egg remains (Veterovata): principles and applications. Journal of Vertebrate Paleontology, 16:763-769.

Mikhailov, K. 1997. Fossil and recent eggshell in amniotic vertebrates: Fine structure, comparative morphology and classification. Special Papers in Palaeontology, 56:1-80.

Moore, D. and R. Reynolds. 1989. X-ray diffraction and the identification and analysis of clay minerals. Oxford University Press, Oxford, 35-64 pp.

Mudge, M. 1970. Origin of the disturbed belt in Northwestern Montana. Geological Society of America Bulletin 81:377-392.

Mueller-Towe, I., P. Sander, H. Schuller, and D. Thies. 2002. Hatching and infilling of dinosaur eggs as revealed by computed tomography. Palaeontographica 267:168.

Nichols, G. 1999. Sedimentology and Stratigraphy. Wiley-Blackwell. West Sussex, UK, 120-121 pp.

Packard, G., T. Taigen, M. Packard, and R. Shuman. 1979. Water-vapor conductance of testudinian and crocodilian eggs (Class Reptilia). Respiration Physiology 38:1–10.

Quinn, B. 1994. Fossilized eggshell preparation. In Leiggi, P. and May, P. (eds): Vertebrate Paleontological Techniques 1:146-153.

Retallack, G. 1990. Soils of the Past. Unwin Hyman, Boston, pp. 520.

Roberts, E. and M. Hendrix. 2000. Taphonomy of a petrified forest in the Two Medicine Formation (Campanian), Northwest Montana: implications for palinspastic restoration of the Boulder Batholith and Elkhorn Mountain Volcanics: Palaios 15:476-482.

Rogers, R. 1998. Sequence analysis of the Upper Cretaceous Two Medicine and Judith River formations, Montana; nonmarine response to the Claggett and Bearpaw marine cycles: Journal of Sedimentary Research 68:615-631.

Rogers, R., C. Swisher III, and J. Horner. 1993. 40Ar/39Ar Age and correlation of the non-marine Two Medicine Formation (Upper Cretaceous), Northwestern Montana: Canadian Journal of Earth Sciences 30:1066-1075.

Rokitka, M. and H. Rahn. 1987. Regional differences in shell conductance and pore density of avian eggs: Respiration Physiology 68:371-376.

Sabath, K. 1991. Upper Cretaceous amniotic eggs from the Gobi Desert. Acta Palaeontologica Polonica 36:151–192.

Sander, P., C. Peitz, F. Jackson and L, Chiappe. 2008. Upper Cretaceous titanosaur nesting sites and their implications for sauropod dinosaur reproductive biology. Palaeontographica 284:69–107.

Seymour, R. 1979. Dinosaur eggs: gas conductance through the shell, water loss during incubation and clutch size. Paleobiology 5:1-11.

Seymour, R. and R. Ackerman. 1980. Adaptions to underground nesting in birds and reptiles: Integrative and Comparative Biology, 20:437-447.

Seymour, R., D. Vleck, and C. Vleck. 1986. Gas exchange in the incubation mounds of megapode birds. Journal of Comparative Physiology 156:773-782.

Seymour, R., D. Vleck, C. Vleck, and D. Booth. 1987. Water relations of buried eggs of mound building birds. Journal of Comparative Physiology 157:413-422.

Thompson, M. B. 1985. Functional significance of the opaque white patch in eggs of *Emydura macquarii*. In B. Grigg, R. Shine, and H. Ehmann (eds): Biology of Australian Frogs and Reptiles. Royal Zoological Society, New South Wales, Sydney. 387–395 pp.

Varricchio, D., F. Jackson, J. Borkowski and J. Horner. 1997. Nest and egg clutches of the dinosaur *Troodon formosus* and the evolution of avian reproductive traits. Nature 385:247-250.

Varricchio, D., F. Jackson, and C. Trueman, C. 1999. A nesting trace with eggs for the Cretaceous Theropod Dinosaur *Troodon formosus*. Journal of Vertebrate Paleontology 19:91-100.

Vejmelek, L., and S. Smithson. 1995. Seismic reflection profiling in the Boulder batholith, Montana. Geology, 23: 811-814.

Vila, B., A. Galobart, O. Oms, B. Poza, and A. Bravo. 2009. Assessing the nesting strategies of Late Cretaceous titanosaurs: 3-D clutch geometry from a new *megaloolithid* eggsite. Lethaia, 10:1502-3931.

Williams, D., R. Seymour, P. Kerourio. 1984. Structure of fossil dinosaur eggshell from the Aix Basin, France. Palaeogeography, Palaeoclimatology, Palaeoecology 45:23-37.

Zelenitsky, D., L. Hills, P. Currie. 1996. Parataxanomic classification of ornithoid eggshell fragments from the Oldman Formation (Judith River Group; Upper Cretaceous), southern Alberta. Canadian Journal of Earth Sciences 33:1655-1667.

Zelenitsky, D., S. Modesto, P. Currie. 2002. Bird-like characteristics of troodontid theropod eggshell. Cretaceous Research 23:297-305.

APPENDIX A

TABLES

Table 1. Egg and rock specimens.

Egg Specimen #	Locality	Description
MOR 326A	Egg Mtn	Egg from clutch of 3
MOR 326B	Egg Mtn	Egg from clutch of 3
MOR 326C	Egg Mtn	Egg from clutch of 3
MOR 301B	Egg Mtn	Egg found associated with MOR 301A
YPM-PU 22544	Egg Mtn	Isolated egg
MOR 3062A	Flaming Cliffs	Egg from eggshell concentration in MOR 3062 trace
Rocks		
MOR 3062-S-U3	Flaming Cliffs	Red mudstone truncated by MOR 3062 nesting trace
MOR 3062-S-N	Flaming Cliffs	Nodules from within MOR 3062-S-U3
MOR 3062-F1	Flaming Cliffs	Green mudstone from the base of the MOR 3062 trace
MOR 3062-S-O	Flaming Cliffs	Horizontal layer of organic material from within trace
MOR 3062-S-F2	Flaming Cliffs	Mottled mudstone above organic layer, within the trace

Table 2. Six eggs showing completeness by region: tapering pole, equator, and wide pole.

Eggs	Tapering Pole	Equator	Wide Pole
MOR 326A	Complete	Complete	Incomplete
MOR 326B	Complete	Complete	Incomplete
MOR 326C	Complete	Complete	Incomplete
MOR 301B	Incomplete	Complete	Complete
YPM-PU 22544	Complete	Complete	Complete
MOR 3062A	Complete	Complete	Complete

Table 3. Measurements from tangential thin sections. T=Tapering Pole, E=Equator, W=Wide Pole.

Sample number	Region	Total area reviewed	Number of pores observed	Individual pore areas in mm^2	Average Pore area in mm^2
MOR 326A	T	6 mm^2	2	.003, .005	0.004
	E	13 mm^2	11	.010, .008, .009, .005, .007, .002, .005, .002, .002, .002, .002	0.005
	W	13 mm^2	8	.013, .008, .011, .005, .005, .005, .006, .002	0.007
MOR 326B	T	5 mm^2	2	.012, .007	0.01
	E	34 mm^2	20	.003, .008, .009, .007, .003, .008, .003, .004, .005, .005, .014, .014, .010, .003, .006, .005, .005, .008, .007, .009	0.007
	W	20 mm^2	6	.009, .003, .006, .008, .007, .013	0.008
MOR 326C	T	18 mm^2	4	.009, .007, .006, .004	0.007
	E	2 mm^2	2	.005, .006	0.006
	W	24 mm^2	6	.014, .008, .003	0.01
MOR 301B	T	6 mm^2	2	.002, .006	0.004
	E	30 mm^2	20	.015, .007, .006, .002, .002, .005, .002, .004, .005, .005, .005, .005, .003, .005, .002, .003, .010, .006, .002, .008	0.005
	W	10 mm^2	7	.012, .022, .005, .008, .006, .011, .004,	0.01
YPM-PU 22544	T	9 mm^2	4	.005, .006, .006, .005	0.006
	E	26 mm^2	7	.009, .011, .018, .005, .003, .008, .006	0.008
	W	14 mm^2	3	.006, .013, .010	0.009
MOR 3062	T	19 mm^2	2	.005, .004	0.005
	E	28 mm^2	4	.012, .010, .015, .014	0.013
	W	20 mm^2	7	.006, .007, .004, .012, .005, .003, .005	0.006

Table 4. Description of formula and source variables and constants.

Variable/ Constant	Description	Units	Formula	Source	Data
L	Egg length	mm	Data	Data	120
B	Egg breadth	mm	Data	Data	55
V	Egg volume	mm^3	$V=0.51(L\ xB^2)$	Hoyt (1987)	$1.85x10^5$
M	Egg mass	g	$M=\rho$ x V	Geometry	199.94
ρ	Egg density	g/mm^3	From avian data	Ar et al. (1974)	1.08
L_s	Shell thickness	mm	Data	Data	*****
A_s	Surface area	mm^2	$A_s = 4.928\ V^{0.668}$	Ar et al. (1974)	*****
D	Pore density	Number per mm^2	Data	Data	*****
N	Number of pores per egg	#	$N = D\ x\ A_s$	Deeming 2006	*****
r	Pore radius	mm	Data	Geometry	*****
A_p	Total pore area	cm^2/egg	$A_p = A\ x\ N$	Deeming 2006	*****
% pore area	Pore area to surface area	%	$(A_p/A_s)\ x\ 100$	Data	*****
A	Mean indiv. pore area	mm^2	$A = \pi r^2$	Geometry	*****
GH2O	Water vapor conductance	mgH2O/ (day Torr)	$\dot{G}H2O = A_p(.447\ xL_s)^{-1}$	Ar and Rahn (1985)	*****
$_pGH2O$	GH2O per pore	µg/ (dayTorr pore)	$pGH2O = \dot{G}H2O\ x\ N^{-1}$	Deeming 2006	*****
Predicted GH2O	GH2O for eq. Mass bird	mgH2O/ (day Torr)	Predicted $GH2O= .3786\ x\ M^{.818}$	Jackson et al. (2008)	*****
c	Constant from empirical avian data	$1.56x10^9$ sec mg $day^{-1}mol^{-1}$	Constant	Ar et al. (1974)	$1.56x10^9$ sec mg $day^{-1}mol^{-1}$
R	Universal gas constant	$6.24\ x10^4$ cm^3 Torr $mol^{-1}K^{-1}$	Constant	Ar et al. (1974)	$6.24\ x10^4$ cm^3 Torr $mol^{-1}K^{-1}$
T	Temperature	303° K (30° C)	Constant	Ar et al. (1974)	303° K (30° C)
dH_2O	Diffusion coefficient for water vapor	0.292 cm^2 sec^{-1}	Constant	Ar et al. (1974)	0.292 cm^2 sec^{-1}

Table 5. Regional calculations for variables of GH2O.

Specimen	Sampling Region	L	B	V	M	ρ	L_s (mm)	A_s (mm^2)	D #/mm^2	N (Pores/egg)	A_p (cm^2/egg)	% pore area	A	~ GH2O	$_pGH2O$
MOR 326A	Tapering	120	55	$1.85x10^5$	199.94	1.08	0.84	16118	0.34	5480	21.92	0.14	0.04	54.97	0.010
	Equator	120	55	$1.85x10^5$	199.94	1.08	0.88	16118	0.85	13700	68.50	0.42	0.05	163.37	0.012
	Wide	120	55	$1.85x10^5$	199.94	1.08	0.89	16118	0.60	9671	65.76	0.41	0.07	155.25	0.016
MOR 326B	Tapering	120	55	$1.85x10^5$	199.94	1.08	0.89	16118	0.40	6447	61.25	0.38	0.10	145.92	0.023
	Equator	120	55	$1.85x10^5$	199.94	1.08	0.95	16118	0.58	9348	63.57	0.39	0.07	140.43	0.015
	Wide	120	55	$1.85x10^5$	199.94	1.08	0.97	16118	0.31	4997	37.98	0.24	0.08	81.92	0.016
MOR 326C	Tapering	120	55	$1.85x10^5$	199.94	1.08	0.99	16118	0.22	3546	23.05	0.14	0.07	48.76	0.014
	Equator	120	55	$1.85x10^5$	199.94	1.08	0.88	16118	1.59	25628	153.77	0.95	0.06	365.91	0.014
	Wide	120	55	$1.85x10^5$	199.94	1.08	0.92	16118	0.25	4030	40.30	0.25	0.10	91.83	0.022
MOR 301B	Tapering	120	55	$1.85x10^5$	199.94	1.08	0.85	16118	0.31	4997	19.99	0.12	0.04	49.25	0.010
	Equator	120	55	$1.85x10^5$	199.94	1.08	0.86	16118	0.66	10638	53.19	0.33	0.05	129.21	0.012
	Wide	120	55	$1.85x10^5$	199.94	1.08	0.92	16118	0.70	11283	109.45	0.68	0.10	250.22	0.022
PU 22544	Tapering	120	55	$1.85x10^5$	199.94	1.08	0.64	16118	0.44	7091	39.00	0.24	0.06	128.56	0.018
	Equator	120	55	$1.85x10^5$	199.94	1.08	0.90	16118	0.27	4352	33.51	0.21	0.08	77.71	0.018
	Wide	120	55	$1.85x10^5$	199.94	1.08	1.08	16118	0.21	3385	30.47	0.19	0.09	59.37	0.018
MOR 3062	Tapering	120	55	$1.85x10^5$	199.94	1.08	0.81	16118	0.10	1612	7.25	0.05	0.05	18.88	0.012
	Equator	120	55	$1.85x10^5$	199.94	1.08	0.66	16118	0.14	2257	29.34	0.18	0.13	94.20	0.042
	Wide	120	55	$1.85x10^5$	199.94	1.08	0.79	16118	0.35	5641	33.85	0.21	0.06	89.72	0.016

Table 6. Regional measurements of microstructures for all six eggs. CL=continuous layer. ML=mammillary layer.

Specimen	Sampling Region	CL (mm)	ML (mm)	ML+CL (mm)	ML+CL w/o node (mm)	mm between ML cones	ML:CL w/o node
MOR 326A	Tapering	0.70	0.13	0.84	0.84	0.15	01:05.29
	Equator	0.75	0.13	1.02	0.90	0.23	01:05.81
	Wide	0.79	0.10	1.11	0.89	0.23	01:08.45
MOR 326B	Tapering	0.73	0.15	1.00	0.88	0.22	01:04.87
	Equator	0.84	0.11	1.18	0.95	0.17	01:07.90
	Wide	0.85	0.12	1.19	0.97	0.16	01:06.97
MOR 326C	Tapering	0.85	0.14	0.99	0.99	0.19	01:06.18
	Equator	0.80	0.08	1.10	0.88	0.12	01:09.74
	Wide	0.80	0.11	1.14	0.92	0.21	01:07.07
MOR 301B	Tapering	0.85	Absent	0.88	0.85	NA	ML Absent
	Equator	0.79	0.08	0.98	0.86	0.20	01:10.51
	Wide	0.81	0.11	1.08	0.92	0.16	01:07.34
PU 22544	Tapering	0.57	0.07	0.74	0.64	0.16	01:08.35
	Equator	0.75	0.15	1.07	0.90	0.22	01:05.03
	Wide	0.97	0.10	1.22	1.08	0.09	01:09.45
MOR 3062	Tapering	0.81	Absent	0.82	0.81	NA	ML Absent
	Equator	0.58	0.08	0.65	0.65	0.24	01:07.37
	Wide	0.69	0.11	1.00	0.79	0.22	01:06.46

Table 7. Geochemical characteristics of sediment samples. TOC is total organic carbon.

Sediment Sample	Iron Present	Iron oxidation	Color	TOC	Mineral composition	Elements Present
MOR 3062-S-U3	X	High	Red-brown	0.01%	quartz, calcite, albite, Al silicate	Si, O, Al, K, Mg, Ca, Na, Fe, C, Ti
MOR 3062-S-N	X	Medium	Red-brown	_____	quartz, calcite, albite, Al silicate, gypsum, anhydrite	Si, O, Al, K, Mg, Ca, Na, Fe, C, Ti, S
MOR 3062-S-F1	X	Low	Green	0.08%	quartz, calcite, albite, Al silicate, sepiolite	Si, O, Al, K, Mg, Ca, Na, Fe, C
MOR 3062-S-O	X	Low	Green-black	0.06%	quartz, calcite, albite, Al silicate	Si, O, Al, K, Mg, Ca, Na, Fe, C
MOR 3062-S-F2	X	Medium	Pale Red	_____	_____	_____

Table 8. Table showing egg regions with indication of complete or incomplete mammillary layer. I= Incomplete. C=Complete.

Eggs	**T**	**E**	**W**
MOR 326A	I	C	I
MOR 326B	C	C	I
MOR 326C	C	I	C
MOR 301B	I	C	I
YPM-PU 22544	I	C	I
MOR 3062	I	I	I